# Flow past a sphere up to a Reynolds number of 300

By T. A. JOHNSON and V. C. PATEL

Iowa Institute of Hydraulic Research and Department of Mechanical Engineering, The University of Iowa, Iowa City, IA 52242-1585, USA

The flow of an incompressible viscous fluid past a sphere is investigated numerically and experimentally over flow regimes including steady and unsteady laminar flow at Reynolds numbers of up to 300. Flow-visualization experiments are used to validate the numerical results and to provide additional insight into the behaviour of the flow. Near-wake visualizations are presented for both steady and unsteady flows. Calculations for Reynolds numbers of up to 200 show steady axisymmetric flow and compare well with previous experimental and numerical observations. For Reynolds numbers of 210 to 270, a steady non-axisymmetric regime is found, also in agreement with previous work. To advance the basic understanding of this transition, a symmetry breaking mechanism is proposed based on a detailed analysis of the calculated flow field.

Unsteady flow is calculated at Reynolds numbers greater than 270. The results at a Reynolds number of 300 show a highly organized periodic flow dominated by vortex shedding. An analysis of the calculated vortical structure of the wake reveals a sequence of shed hairpin vortices in combination with a sequence of previously unidentified induced hairpin vortices. The numerical results compare favourably with experimental flow visualizations which, interestingly, fail to reveal the induced vortices. Based on the deduced symmetry-breaking mechanism, an analysis of the unsteady kinematics, and the experimental results, a mechanism driving the transition to unsteady flow is proposed.

## 1. Introduction

The flow of a viscous fluid past a stationary isolated sphere may be considered a simplified case of a general family of immersed bluff-body flows with widespread applications. Like its two-dimensional counterpart, the flow past a cylinder, instabilities are known to generate fully three-dimensional unsteady flow fields in spite of the symmetry of the body. Unlike two-dimensional flows, however, such three-dimensional flows are capable of admitting even more complicated kinematic and vortical interactions and have, therefore, remained less well understood.

The behaviour of the flow past a sphere at varying Reynolds numbers has been studied by a number of researchers. Taneda (1956) used flow visualization methods to study the wake of a sting-mounted sphere for $5 < Re < 300$, where $Re$ is the Reynolds number based on the sphere diameter $D$ and velocity $U_\infty$. He determined that separation from the rear of a sphere occurs at $Re \approx 24$ and results in the generation of an axisymmetric vortex ring. With regard to the stability of the resultant wake, he observed a faint periodic motion, 'with a very long period' at the rear of the vortex ring beginning at $Re = 130$.

Magarvey & Bishop (1961) used dye visualization to reveal the wakes of free-falling drops of an immiscible liquid in water. A qualitative comparison to standard solid sphere wakes is possible, as pointed out by Natarajan & Acrivos (1993), due to the presence of surface-active impurities at the liquid–liquid interface, which hold the drops in a semi-rigid spherical shape, a presumption supported by Winnikow & Chao (1966). The wakes of the liquid spheres exhibited the same vortex ring structure observed by Taneda. However, the rings remained stable and axisymmetric up to $Re = 210$. In the range $210 < Re < 270$, the flow became non-axisymmetric as the ring vortex shifted off-axis and dye was released from the wake in two parallel threads. In contrast to the flow past a circular cylinder, which becomes unsteady upon the loss of symmetry, this double-thread wake was observed to remain steady. By $Re = 270$ the double-thread wake was itself observed to become unstable and eventually vortex loops began shedding from the sphere as so-called hairpin vortices.

The steady non-axisymmetric wake seen behind Magarvey & Bishop's liquid drops for $210 < Re < 270$ has also been observed behind free-falling, fluid-filled spherical shells by Nakamura (1976). It should be noted that the mass of fluid within Nakamura's spherical shells was free to move around, potentially affecting the sphere's motion and the wake development. His wakes remained stable and axisymmetric up to $Re = 190$ at which point he too noted the steady, non-axisymmetric double-thread wake.

Tomboulides (1993) presents numerical results from a spectral element solution of the flow over a sphere for $25 < Re < 10^3$ and with large-eddy simulation at $Re = 2 \times 10^4$. He shows steady axisymmetric flow for $Re < 212$ with initial separation at $Re = 20$. He found a regular bifurcation, i.e. a transition to steady flow, at $Re = 212$. The vorticity of the resulting steady flow field resembled the double-thread wake observed by Magarvey & Bishop at $210 < Re < 270$ and Nakamura at $Re = 190$.

Natarajan & Acrivos (1993) investigated the stability of the axisymmetric sphere flow using a finite-element method. Consistent with the above results, they too found a regular bifurcation at $Re = 210$ and they naturally suggest that this corresponds to the transition from the steady axisymmetric wake to the steady, non-axisymmetric, double-thread wake.

The regime of unsteady vortex shedding from a sphere has received the most attention in the literature. The observed onset of the shedding regime covers the range $290 < Re < 400$. A number of researchers, including Achenbach (1974), Kim & Durbin (1988), and Sakamoto & Haniu (1990), present measurements of the frequencies present in the unsteady wake. At, and in a small range above, the onset of unsteadiness, i.e. up to $Re \approx 420$, a strongly periodic process is indicated by the observation of a single frequency in the wake at a Strouhal number $St$ in the range $0.15 < St < 0.17$. In addition to providing frequency measurements, Achenbach, Sakamoto & Haniu, and Perry & Lim (1978) have shown, with varying detail, visualizations of hairpin vortices shedding from spheres. Sakamoto & Haniu (1990, 1995), in particular, provide fascinating pictures of the hairpin vortices as they form in both uniform and shear flows.

Recent numerical solutions of the unsteady flow past a sphere include that by Shirayama (1992), who solved for the case of flow accelerating from rest to $Re = 500$; Gebing (1994), who solved the unsteady compressible-flow equations at Reynolds numbers of 20 to 1000 and a Mach number of 0.4; and as mentioned above, Tomboulides (1993). Gebing found a loss of axial symmetry by $Re = 300$ and computed unsteady flow at $Re \geqslant 400$. His particle traces at $Re = 400$ show vortex structures resembling the visualization results of Sakamoto & Haniu. Tomboulides
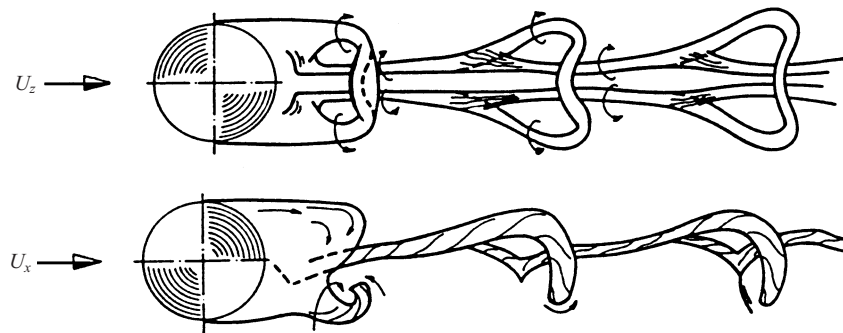
FIGURE 1. Achenbach's (1974) sketch of the wake vortex configuration at $Re = 10^3$.

records the unsteady transition in the range $270 < Re < 285$, which corresponds with the onset of unsteadiness seen by Magarvey & Bishop at $Re = 270$. His isocontours of streamwise vorticity for $Re = 300$ resemble structures visualized in previous experimental studies. Unfortunately, particle traces are not provided for a more appropriate comparison with experiments.

Particularly interesting throughout the literature is that within a small range of the onset of shedding, corresponding to the single frequency range, the visualized hairpin vortices are all shed with the same orientation, forming a ladder-like chain of overlapping loops as sketched by Achenbach and reproduced here in figure 1. Although the presence of a double-sided shedding regime is also observed (see Perry, Lim & Chong 1980) the current work focuses solely on single-sided shedding of the type represented in figure 1. A close examination of figure 1 raises some basic questions that have yet to be addressed. First, and most fundamentally, by what mechanism are the vortices formed and shed? There is a definite difference between this three-dimensional structure and the alternately shed vortices behind a two-dimensional body. Experimental visualizations have provided some insight into the geometry of the process but finer details and the actual dynamics remain unclear. In addition, the few computational solutions available have not been satisfactorily applied to clearly reveal these details. Secondly, if the hairpin vortices are continually shed into the wake with the same orientation, how is the associated transverse circulation in the wake bounded? Clearly, the total circulation of the field is not indicated by the visualized vortices. Finally, in what way are the successive hairpins connected? As depicted in figure 1, with the legs of one vortex merging with the head of the next, there would be problems with the topology of the flow vectors.

The current work attempts to answer these questions by numerically solving the flow in a three-dimensional, time-dependent fashion and analysing the flow dynamics and structure for each of the aforementioned regimes. Section 2 of this paper describes the numerical method used to solve the Navier–Stokes equations. Section 3 gives an overview of the experimental set-up used to obtain flow-visualization pictures, which are used to corroborate the numerical results. The numerical results for the first regime, that of steady axisymmetric flow, are presented in §4. The results for the second regime, steady non-axisymmetric flow, are presented in §5 along with a comparison to some experimental results. Also, a description of the mechanism driving the shift from the first to the second regime is proposed. In §6 the results for unsteady flow are considered and a mechanism driving the unsteady transition and shedding process is presented. In addition, a new vortical feature present in the sphere wake is identified.

## 2. Numerical method

The numerical method used in this study is presented in detail in Johnson (1996). The method incorporates a dual time-stepping formulation with local pseudo-time stepping. A four-stage Runge–Kutta method is used to integrate the momentum equations in pseudo-time, while a pressure Poisson equation is formulated to satisfy the continuity equation.

### 2.1. *Numerical formulation*

The Runge–Kutta integration of the momentum equations in pseudo-time may be written as

$$u_i^l = u_i^n - \alpha_l \Delta\tau(US_i^{l-1} + C_i^{l-1} - V_i^l + \nabla_i p^{n+1}), \tag{1}$$

where $i = 1, 2$ and $3$ denote the three components of velocity, and $US$, $C$, $V$ and $\boldsymbol{\nabla}p$ represent the temporal acceleration, convective, viscous, and pressure gradient terms, respectively. The superscripts $n$ and $n+1$ represent, respectively, the beginning and end of one complete pseudo-time step. The superscirpt $l$ represents the Runge–Kutta stage: 1–4 for the four-stage method, where $l = 4$ corresponds to $n+1$. The parameters $\alpha_l$ are the Runge–Kutta coefficients; 1/4, 1/3, 1/2 and 1 for a four-stage scheme, and $\Delta\tau$ is the pseudo-time step. On the right-hand side the unsteady term $US_i^{l-1}$ is given by

$$US_i^{l-1} = \frac{3u_i^{l-1} - 4u_i^m + u_i^{m-1}}{2\Delta t} \tag{2}$$

which is simply a second-order backward difference for the time derivative of $u_i$ calculated explicitly at the previous Runge–Kutta stage $l-1$. The superscript $m$ in (2) represents the last converged physical time step and $\Delta t$ is the physical time increment. Both the viscous terms and the pressure gradient terms are discretized using second-order central differences while the convective terms are discretized using second-order upwind differences. The convective terms, just like the unsteady terms, are computed explicitly at the previous integration stage. The viscous terms are handled implicitly through the application of an implicit smoothing operator to ease the stability restrictions associated with an explicit formulation. The implicit smoothing procedure is given as

$$\left(1 - \frac{\alpha_l \Delta\tau}{Re}\nabla^2 - \epsilon\nabla^2\right)\mathrm{RHS}_i^* = -\alpha_l \Delta\tau(US_i^{l-1} + C_i^{l-1} - V_i^n + \nabla_i p^{n+1}) \equiv \mathrm{RHS}, \tag{3}$$

where RHS is defined as the unsmoothed forcing function and $\mathrm{RHS}_i^*$ is the smoothed right-hand side. The integration of the momentum equations is then given by

$$u_i^l = u_i^n + \mathrm{RHS}_i^*. \tag{4}$$

The smoothing operator on the left-hand side of (3) contains the implicit viscous operator, proportional to the inverse of the Reynolds number, plus an additional smoothing term of strength $\epsilon$ for added control of the stability. As defined, RHS does not contain an implicit viscous term (note the superscript $n$) and is used as shown below in the pressure equation.

The pressure, which appears implicitly in (3), is obtained from a Poisson-like equation for $\Delta p = p^{n+1} - p^n$, arising from the enforcement of a divergence-free condition on the advanced velocity field of (4). With the addition of a discrete pseudo-

time derivative for iterative advancement and a dissipation term to control decoupling, the equation for the pressure increment is given as

$$-\beta\frac{\Delta p^n}{\Delta\tau} + \boldsymbol{\nabla}\cdot[\Delta\tau\boldsymbol{\nabla}(\Delta p^n)] = \frac{1}{\alpha_l}\boldsymbol{\nabla}\cdot[\boldsymbol{u}^n + \text{RHS}] + \text{DISS}. \qquad (5)$$

The parameter $\beta$ sets the ratio between the pressure equation's pseudo-time step and that of the momentum equations. An effective value for $\beta$ was found to be 0.5, giving the pressure equation a pseudo-time step of 2 times that of the momentum equation. Note that RHS, instead of RHS*, is used on the right-hand side of (5) and contains the explicit form of the viscous term since the pressure equation is solved prior to implicit smoothing. Also notice that the divergence of $u^n$ is retained on ther right-hand side in order to dissipate any errors in continuity from previous iteration levels. The dissipation term DISS is added to eliminate odd–even decoupling of the pressure field and is given by

$$\text{DISS} = \epsilon(\tilde{\nabla}^2_{5pt} - \tilde{\nabla}^2_{3pt})p, \qquad (6)$$

where $\epsilon$ is some small multiplier and the $\tilde{\nabla}^2$ operators are given by

$$\tilde{\nabla}^2 = \boldsymbol{\nabla}\cdot[\Delta\tau\boldsymbol{\nabla}p] \qquad (7)$$

with second-order divergence and gradient operators applied directly at the nodes for $\tilde{\nabla}^2_{5pt}$ and at the half-nodes for $\tilde{\nabla}^2_{3pt}$. The dissipation therefore effectively replaces a portion of the five-point pressure gradient term, which allows decoupling, with a three-point pressure gradient term, which eliminates decoupling but is inconsistent with a nodal solution of the momentum equations. It is important to notice that at convergence, as RHS and the left-hand side of (5) go to zero, the divergence of the velocity is driven not to zero but rather to $-\text{DISS}$. However, keeping $\epsilon$ on the order of $\Delta\tau$ ensures that the error in continuity is at most second order. For the case of a driven cavity, Sotiropoulos & Abdallah (1991) show that $\epsilon = 0.1$ is sufficient to eliminate decoupling while keeping the error incurred in the continuity equation on the order of $10^{-3}$.

In the solution of (3) and (5) the approximate factorization method of Beam & Warming (1978) is used to reduce the left-hand sides to three one-dimensional operators, which are easily inverted with the Thomas algorithm.

The physical time step in (2) is selected on the basis of the desired temporal accuracy. To efficiently obtain steady-state solutions in flow regimes where they are meaningful $\Delta t$ was set to infinity. The pseudo-time step $\Delta\tau$ is limited by stability considerations and was selected according to

$$\Delta\tau = \min\left[\frac{\text{CFL}\,\Delta x}{U_\infty}, \text{VN}\,Re\,\Delta x^2, \Delta t\right], \qquad (8)$$

where CFL and VN are the Courant–Friedrichs–Lewy and von Neumann numbers and $\Delta x$ is the discrete spatial increment of the numerical grid. Optimum values for both the CFL and VN numbers were obtained through numerical experimentation. Equation (8) simply ensures that the numerical solution does not try to overstep any convective, viscous, or temporal disturbances.

Converged solutions were obtained by integrating (4) and (5) in pseudo-time until both RHS* in (4) and the right-hand side of (5) were less than $10^{-5}$. This criterion ensures that the momentum equation terms and the continuity/dissipation terms are balanced to within the method's second-order accurate design.
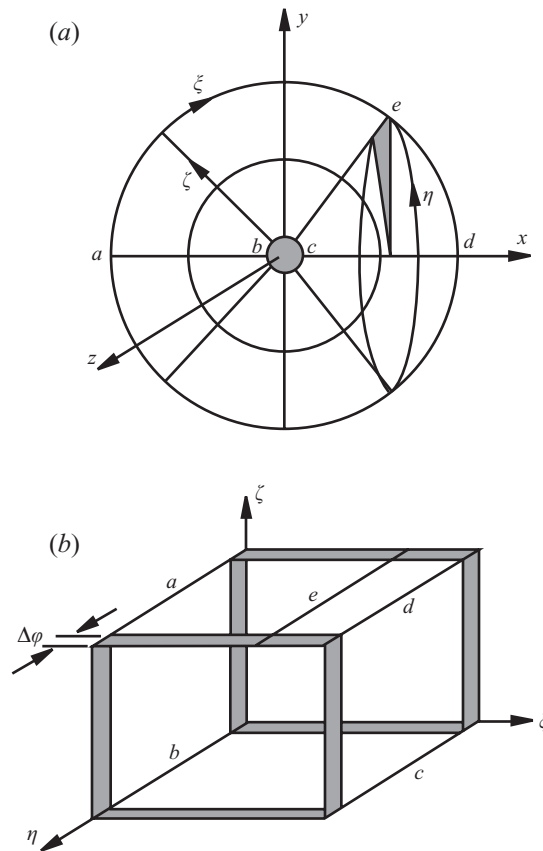
FIGURE 2. Computational grid topology: (*a*) physical space; (*b*) computational space.

## 2.2. *Numerical grid*

The sphere lends itself naturally to the generation of a numerical grid following a spherical coordinate system. Figure 2 shows the grid topology in both physical and computational space. The grid is an O-O type where the numerical coordinates ($\xi, \eta, \zeta$), lie along the standard spherical coordinates ($\Theta$, , $r$). The coordinate transformation is given as follows:

$$\Theta = \pi \frac{(\xi - 1)}{(\xi_{max} - 1)}, \qquad = 2\pi \frac{(\eta - 1)}{(\eta_{max} - 2)}, \quad r = 0.5 \exp\{k_1(\zeta - 1) + k_2(\zeta - 1)^2\} \qquad (9)$$

with the Cartesian coordinates ($x, y, z$) given as

$$x = -r \cos\Theta, \quad y = r \sin\Theta \cos \quad , \quad z = r \sin\Theta \sin \quad , \qquad (10)$$

where $(1, 1, 1) \leqslant (\xi, \eta, \zeta) \leqslant (\xi_{max}, \eta_{max}, \zeta_{max})$. The grid dimensions $(\xi_{max}, \eta_{max}, \zeta_{max})$ were $(101, 42, 101)$. The polar coordinate $\Theta$ spans linearly from 0 at $\xi = 1$, on the upstream negative-*x*-axis, to $\pi$ at $\xi = \xi_{max}$, on the downstream positive-*x*-axis. The azimuthal coordinate  encircles the axis spanning linearly from 0 to $2\pi + \Delta$ . The $\Delta$ overlap is indicated in figure 2(*a*) with a shaded arc and allows for periodic boundary conditions in the $\eta$-direction. In this way, no boundary conditions in the $\eta$-direction have to be prescribed.

In the radial direction, *r* goes from the surface of the sphere at $r = 0.5$, to 15 diameters from the sphere's centre. Early tests with grid size showed little change in the

flow solution at Reynolds numbers less than 100 from extending the grid beyond 15 diameters, i.e. the rear stagnation point pressure coefficient differed by less than 1.2% with an increase in maximum grid radius to 20 sphere diameters. At a grid radius of 15 diameters the effective blockage ratio, defined as the sphere's frontal area divided by the computational grid's frontal area, is about 0.11%. The coefficients $k_1$ and $k_2$ are used to fix the maximum radial dimension, $r = 15$, and to stretch the grid toward the body surface. The amount of stretching was chosen to place at least ten grid points within the boundary layer at the front stagnation point. The approximate boundary layer thickness at the sphere's stagnation point is given in Schlichting (1979) as $\delta = 1.13/Re^{1/2}$, where $\delta$ is the boundary layer thickness non-dimensionalized by the diameter of the sphere. The minimum grid spacing, adjacent to the sphere, was 0.005 with a stretching ratio of less than 1.06.

Grid dependency checks and Richardson extrapolation techniques were used to provide an indication as to the required grid size and the approximate order of accuracy of the method. The results, which are provided in Johnson (1996), indicate an order of accuracy of approximately 1.7 and show that reasonable grid independence is achieved on a $(101, 42, 101)$ grid.

### 2.3. Boundary conditions

On the surface of the sphere, the no-slip condition is applied:

$$u = v = w = 0.$$

At $\zeta = \zeta_{max}$, the grid surface is a combination inflow and outflow boundary. In figure 2(a) for values of $\xi$ between points $a$ and $e$, free-stream boundary conditions are applied:

$$u = 1, \quad v = w = 0.$$

In the region $e < \xi < d$, the $\zeta_{max}$ surface is defined as an outflow boundary to where velocities must be extrapolated. All three velocities were extrapolated using a second-order backward difference approximation for a zero second derivative in the $\zeta$-direction:

$$u_{i,\zeta_{max}} = \frac{5u_{i,\zeta-1} - 4u_{i,\zeta-2} + u_{i,\zeta-3}}{2}, \quad i = 1, 2, 3. \tag{11}$$

Point $e$ was set at 70° off the downstream axis, well past the point at which the solution was found to be sensitive to variations in the point's location.

The $\xi = 1$ and $\xi = \xi_{max}$ boundaries correspond to the axes of the spherical grid. Along these axes the velocities were taken to be azimuthal averages of second-order Adams–Bashforth extrapolations, i.e. for $\xi = \xi_{max}$

$$u_{1,\xi_{max}} = \frac{1}{\eta_{max} - 2} \sum_{\eta=1}^{\eta_{max}-2} \left( \frac{4u_{i,\xi_{max}-1} - u_{i,\xi_{max}-2}}{3} \right). \tag{12}$$

The analogous equation for $\xi = 1$ is obtained using forward differences. Note that the summation is taken only for $\eta$ from 1 to $\eta_{max-2}$ since these comprise the only unique points in the $\eta$-direction. With the grid overlap in the $\eta$-direction, points at $\eta_{max}$ are equivalent to points at $\eta = 2$, and points at $\eta_{max-1}$ to points at $\eta = 1$. Therefore, on the $\eta = 1$ and $\eta = \eta_{max}$ boundaries, periodic conditions are imposed:

$$u_{i,\eta=1} = u_{i,\eta_{max}-2}, \quad u_{i,\eta_{max}} = u_{i,\eta=2}. \tag{13}$$

At the $\xi$ and $\eta$ boundaries, the pressure boundary conditions are exactly the same as the velocity boundary conditions, i.e. (12) and (13) for $p$ instead of $u_i$. At the $\zeta = 1$ and $\zeta = \zeta_{max}$ boundaries the pressure is simply extrapolated from the interior points as follows:

$$p_{1(\zeta_{max})} = p_{\zeta \pm 1} + \frac{\Delta \bar{x}_{\zeta \pm 1}}{\Delta \bar{x}_\zeta}(p_{\zeta \pm 1} - p_{\zeta \pm 2}), \tag{14}$$

where the $\pm$ refers to $+$ for $\zeta = 1$ and $-$ for $\zeta = \zeta_{max}$ and

$$\Delta \bar{x}_\zeta = \{(x_{\zeta+1} - x_\zeta)^2 + (y_{\zeta+1} - y_\zeta)^2 + (z_{\zeta+1} - z_\zeta)^2\}^{1/2}. \tag{15}$$

## 3. Experimental method

In order to provide some corroborating evidence for the simulation results, dye-injection experiments were performed in the wake of a sphere towed through water. The water tank used for the experiments is 3.66 m long, 61 cm wide and 76 cm deep. The bottom, sides, and ends are made of 1.27 cm glass for optical access. Two rails are mounted beneath the tank upon which a towing carriage rides powered by a screw drive extending the length of the tank. The drive provides a velocity range of 0.5–5 cm s$^{-1}$. In all cases the acceleration of the carriage to a uniform velocity was complete within 10 cm of travel, so no results were obtained before 60 cm of travel, allowing transient effects to be ignored.

A second set of rails is mounted along the top sides of the tank to support a smaller carriage which held the sphere model and support struts. The smaller carriage was used in order to minimize any oscillations generated by the larger carriage. The small carriage is linked to the large carriage via a rubberized connector designed to reduce the transmission of vibrations. Two sets of struts, one front and one back, are mounted on the small carriage 44 cm apart. Each set supports a 50 cm diameter anchoring ring fitted with small holes located every 10° around its perimeter to anchor the support wire for the model. This set-up allows the orientation of both the tow-tank models and their support wires to be rotated as a unit relative to the tank reference system thereby allowing variable viewing angles of the flow field. It was hoped that by changing the azimuthal orientation of the sphere support wires, the orientation of the non-axisymmetric wake could be controlled. Unfortunately, this degree of flow control was not consistently realized: the small disturbances from the wires were either not sufficient to affect the development of the wake or were overwhelmed by other outside disturbances.

The degree of the disturbances produced by the struts and anchoring rings was checked by injecting dye into the tank and traversing the empty support structure, without the sphere or support wire. The shedding that occurred off the supports was limited to less than 3 cm inside the ring radius. In addition, the dye across the remaining area encircled by the ring was undisturbed by the passing of the supports. Conservatively, from the centre axis of the model mounting volume, a 20 cm radius of water was left undisturbed by the mounting struts and rings.

The model itself was a Plexiglas sphere with a 2.54 cm diameter with an accuracy of $\pm 0.2\%$. With the velocity range of the drive mechanism, this size sphere allowed a Reynolds number range of approximately 125–1250. For mounting the sphere, a 0.02 cm hole was pierced through the sphere's centre using an industrial laser. The sphere was then threaded and glued onto a 0.018 cm stainless steel support wire. The ends of the support wire were attached to small turnbuckle hooks designed to mount

on the anchoring rings in tension to limit spurious motion of the sphere. With the rings separated by 44 cm, the support wire made an angle of 49° relative to the direction of motion.

Propagation of the estimated accuracies of traverse velocity, sphere diameter, and temperature-dependent viscosity give an estimated Reynolds number accuracy of about 3%.

Standard dye injection was used to visualize the wake structure. Although specific details of the wake's structure can be obscured by this approach, the overall shape of the near wake, as well as the downstream behaviour of the far wake, is clearly revealed. Food colouring diluted in water was used as the dye. A very small amount of alcohol was also added to the mixture to produce a neutrally buoyant solution. To visualize the wake, a few millilitres of the dye mixture were injected into the water surrounding the sphere which was then set into motion, passing through and entraining the cloud of dye into its wake. With a camera mounted on the towing carriage, photographs of the wake were taken as the sphere traversed the length of the tank.

## 4. Steady axisymmetric flow

At Reynolds numbers between 20 and approximately 210, the flow is separated, steady, axisymmetric, and topologically similar. As mentioned in §2, the solutions in this steady regime were obtained by setting $\Delta t$ in (2) to infinity in the interest of numerical efficiency. The calculated upper and lower Reynolds number limits of this regime compare well with experimental results of Magarvey & Bishop (1961) and the numerical results of Natarajan & Acrivos (1993) and Tomboulides (1993). Differences exist with the experimental results of Taneda (1956) and Nakamura (1976) who reported waviness in the wake at Reynolds numbers above 130 and 190, respectively.

Streamlines for this regime are shown in figure 3($a$–$d$), which shows the $(x, y)$-planes for Reynolds numbers 50, 100, 150 and 200. In these and all following figures, unless otherwise noted, the flow direction is from left to right. As illustrated in figure 3($b$), the flow is seen to separate from the surface of the sphere at an angle $\Theta_s$ from the front stagnation point and rejoin at a point $x_s$ on the axis of the flow to form a closed separation bubble and a toroidal vortex centred at $(x_c, y_c)$, where the velocity is zero in the sphere's reference frame. For all Reynolds numbers between 20 and 210 the flow structure remains topologically the same with changes only in the separation location, the vortex's position, and the separation bubble length. The numerical results of Pruppacher, Le Clair & Hamiliec (1970), Tomboulides (1993), and Magnaudet, Rivero & Fabre (1995) and the experimental measurements of Taneda (1956) provide data for comparison with the present results. Figure 4 shows good agreement between the current results for separation angle $\Theta_s$ and length $x_s$ and vortex $(x_c, y_c)$ position with the aforementioned results. The only significant deviation in any of the results is in figure 4($b$), where Taneda's separation length at the higher Reynolds numbers is almost 20% lower than the current results and those of Tomboulides.

Further comparison to experimental results can be made with the drag coefficient, given as $C_D = F_x/(\frac{1}{2}\rho U_\infty^2 \pi D^2/4)$, where $F_x$ is the force in the streamwise direction. Roos & Willmarth (1971) provide detailed drag coefficient data which compare well with results given by Allen (1900), Wieselsberger (1922), Schmiedel (1928), Liebster (1928) and Schiller (1930). Figure 5 plots the present study's computed drag coeffiients versus Reynolds number and shows good agreement with the values of Roos & Willmarth.

Contours of the pressure coefficient, defined as $C_P = (P - P_\infty)/\frac{1}{2}\rho U_\infty^2$, are shown in figure 6($a$–$d$), ordered with increasing Reynolds number. Contours are drawn for every
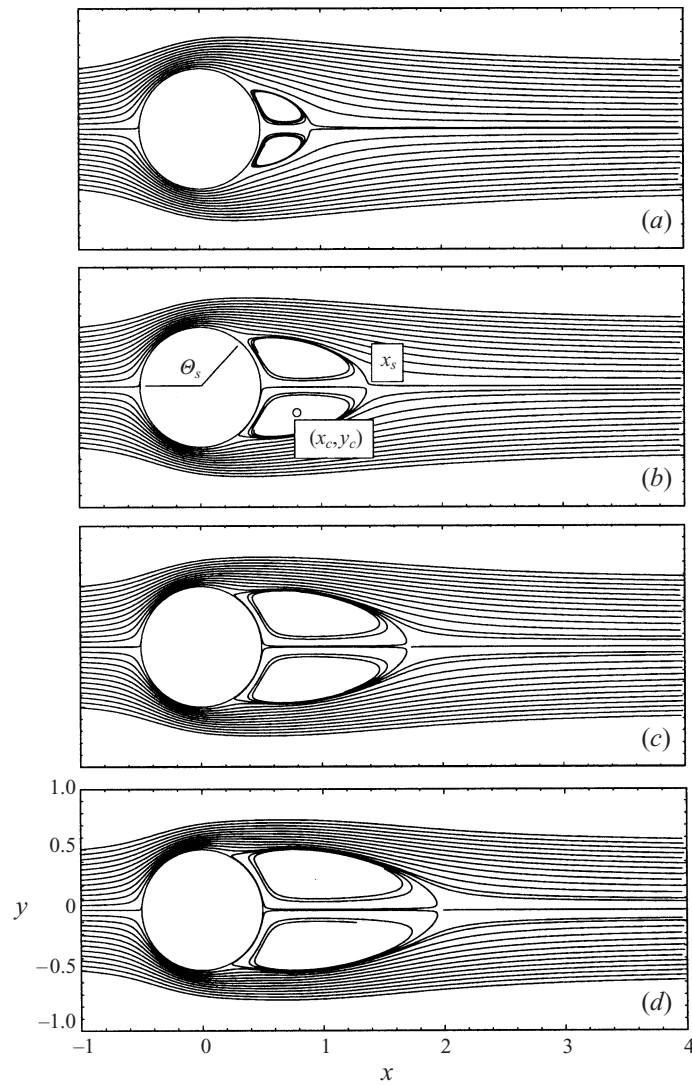
FIGURE 3. Computed axisymmetric streamlines past the sphere:
(*a*) *Re* = 50; (*b*) *Re* = 100; (*c*) *Re* = 150; (*d*) *Re* = 200.

0.04 increment with dashed lines used for negative values. Within the wake, in the vicinity of the toroidal vortex shown in figure 3, it is interesting to note that there is no pressure minimum in the symmetry plane until a Reynolds number of 200. In figure 6(*d*) the closed circles in the wake indicate a pressure minimum located very near the centre of rotation of the toroidal vortex. At Reynolds numbers less than 200 the centrifugal force of the vortex's rotation must be balanced by viscous forces as opposed to a radial pressure gradient.

The evolution of the vorticity field, which for this first regime consists of only an azimuthal component, is illustrated in figure 7(*a*–*d*). Vorticity contours are drawn in increments of 0.5 with negative values indicated by dotted lines. The thinning of the vorticity layer on the surface of the sphere and the increase in the downstream extension of vorticity with Reynolds number is immediately obvious. At Reynolds
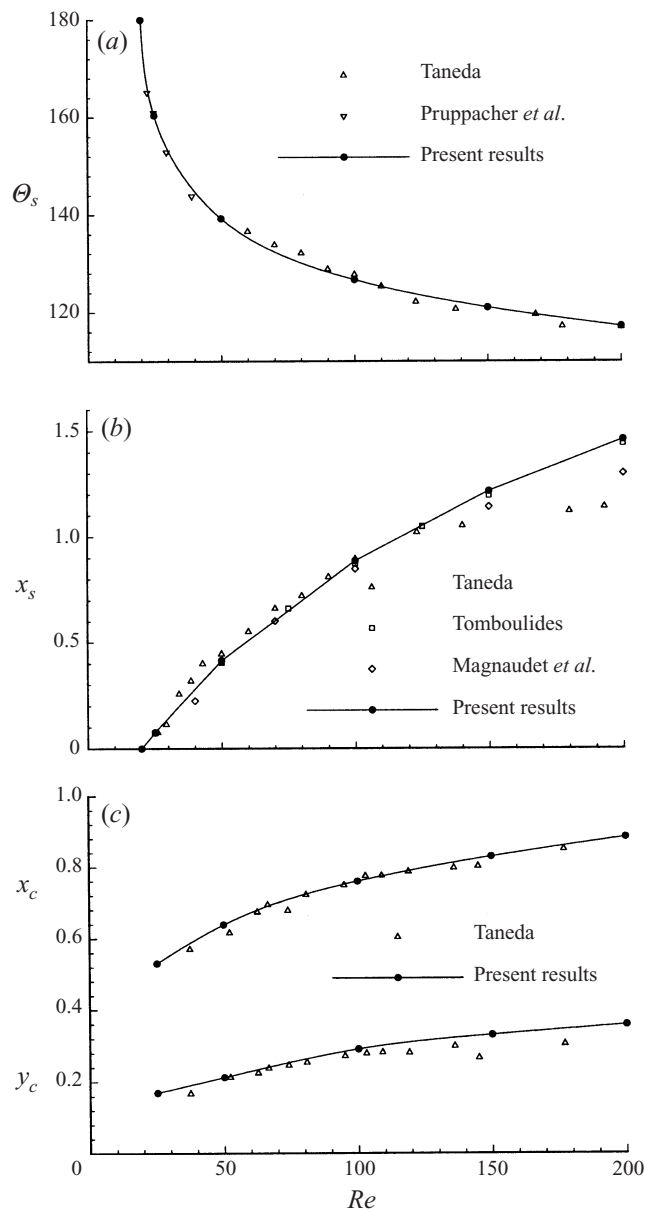
FIGURE 4. Flow geometry versus Reynolds number: (*a*) polar separation angle $\Theta_s$; (*b*) separation length $x_s$; (*c*) vortex position $(x_c, y_c)$.

numbers of 100 and above, the change in sign of the vorticity across the separation point is also obvious. What is not obvious from the vorticity contours, however, is the vortex structure of the wake. Although the existence of the toroidal vortex is clear from the streamline patterns of figure 3, neither the pressure nor the vorticity contours indicate the presence of spiralling streamlines. It is important to understand the vortex structure of the wake since it communicates information on the kinematics of the wake which in turn highlight the dynamic influences governing the flow behaviour.

To address the issue of properly identifying vortical regions, a number of methods have been proposed. Jeong & Hussain (1995) have reviewed these methods, including
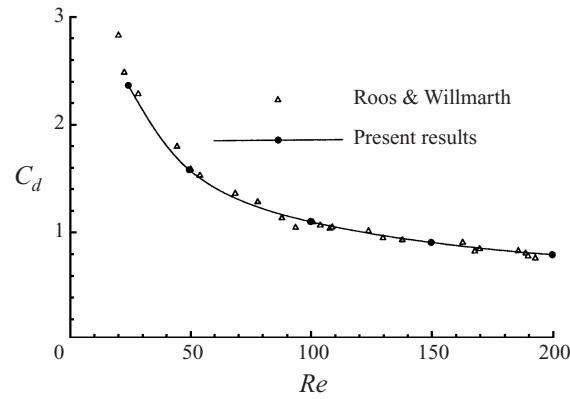
FIGURE 5. Drag coefficient versus Reynolds number.
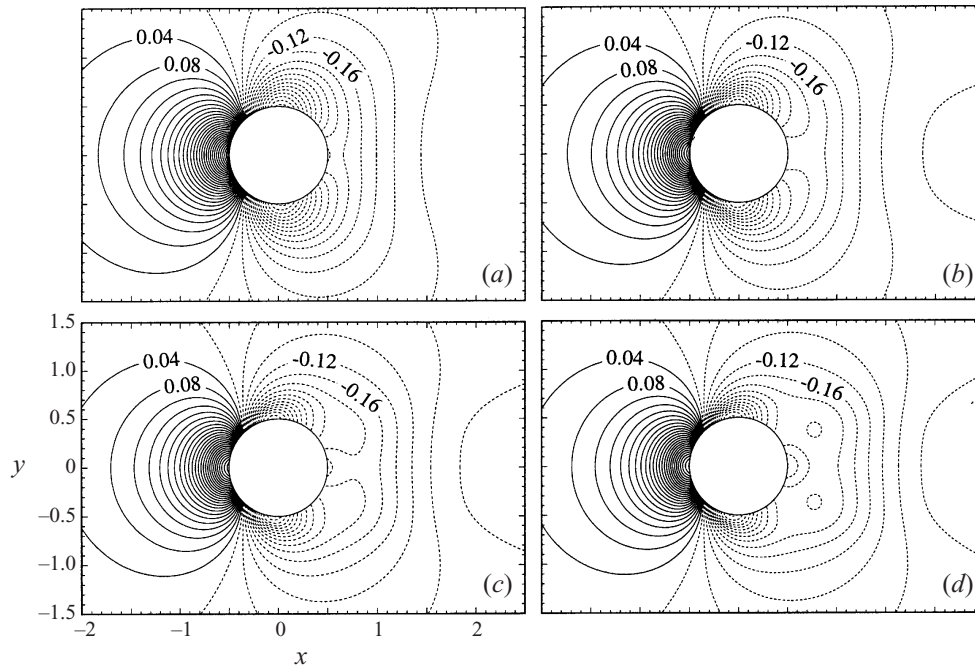


FIGURE 6. Flow field pressure coefficient contours for axisymmetric flow:
(a) $Re = 50$; (b) $Re = 100$; (c) $Re = 150$; (d) $Re = 200$.

those put forth by Hunt, Wray & Moin (1988) and Chong, Perry & Cantwell (1990), and have proposed a new method. They consider the role of the swirling motions in a vortex in generating local pressure minima. The negative of the Hessian of the pressure is given as

$$-\left[\frac{\partial^2 p}{\partial x_i \partial x_j}\right] = \frac{DS_{ij}}{Dt} - \nu \frac{\partial^2 S_{ij}}{\partial x_k \partial x_k} + S_{ik} S_{kj} + \Omega_{ik} \Omega_{kj}, \tag{16}$$

where the rate of strain $S_{ij}$ and rate of rotation $\Omega_{ij}$ tensors are

$$S_{ij} = \frac{1}{2}\left(\frac{\partial u_i}{\partial x_j} + \frac{\partial u_j}{\partial x_i}\right), \quad \Omega_{ij} = \frac{1}{2}\left(\frac{\partial u_i}{\partial x_j} - \frac{\partial u_j}{\partial x_i}\right). \tag{17}$$
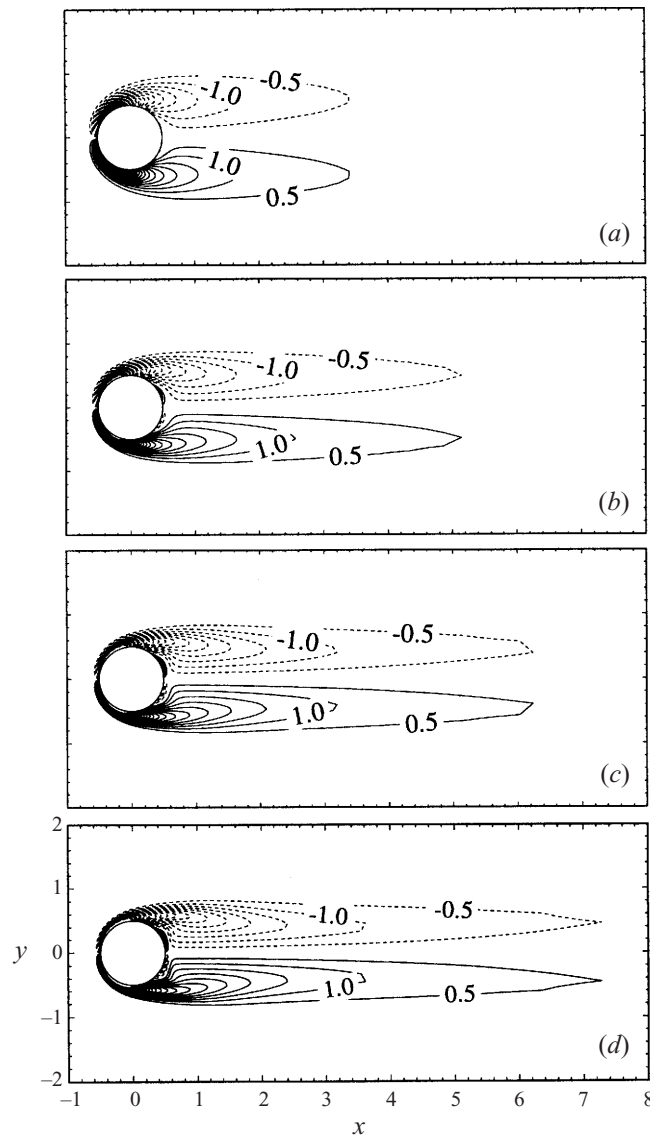
FIGURE 7. Vorticity contours for axisymmetric flow:
(a) $Re = 50$; (b) $Re = 100$; (c) $Re = 150$; (d) $Re = 200$.

Neglecting the influence of the first two terms on the right-hand side of (16), Jeong &
Hussain define a vortex core as a connected region containing two negative eigenvalues
of $\boldsymbol{S}^2 + \boldsymbol{\Omega}^2$, i.e. a local pressure minimum in a plane. Jeong & Hussain provide a
number of examples to illustrate the advantages of this method over others, indicating
a more robust and precise elucidation of the vortical regions. The results of their
method applied to the axisymmetric flow over a sphere are shown in figure 8 for
Reynolds numbers of 25, 100 and 200. There are two regions containing the two
negative eigenvalues of the $\boldsymbol{S}^2 + \boldsymbol{\Omega}^2$ tensor; vortical structures are expected within these
areas.

At a Reynolds number of 25, in figure 8(a), small elliptical regions are located
immediately downstream of the rear stagnation point of the sphere. A comparison with
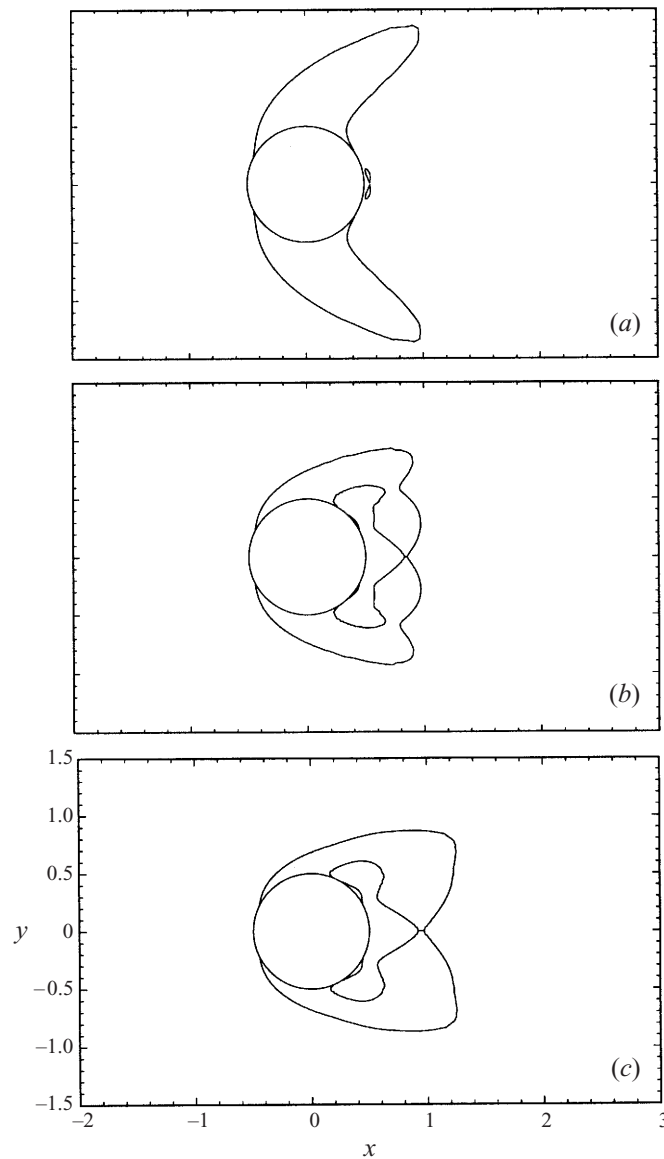
FIGURE 8. Vortical regions as given by Jeong & Hussain's method:
(a) $Re = 25$; (b) $Re = 100$; (c) $Re = 200$.

the streamline patterns of figure 3(a) confirms that these indicate the location of the toroidal vortex in the wake. The large lobes of the contour located above and below the sphere in figure 8(a) do not coincide with any vortical structure apparent in figure 3(a). However, in a reference frame moving with the local velocity, closed streamline orbits do appear in that region, as shown in figure 9. The streamlines in figure 9 are drawn in a reference frame moving to the right at about one-half the speed of the free stream. Note that this reference frame velocity was arbitrarily selected to illustrate this point and that the same effect is apparent for a number of reference velocities. The recirculation patterns, or vortical structures, are a result of the boundary layer moving over the convex surface of the sphere. The same phenomenon can be seen in Van
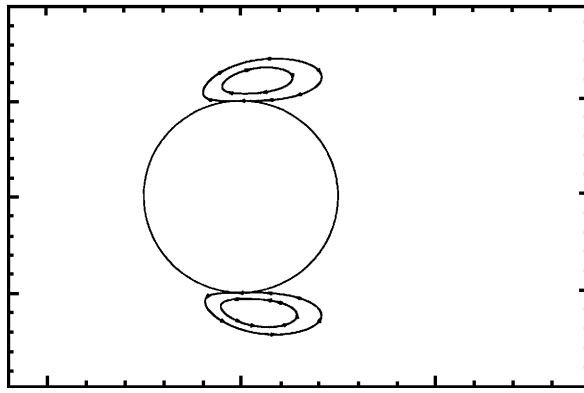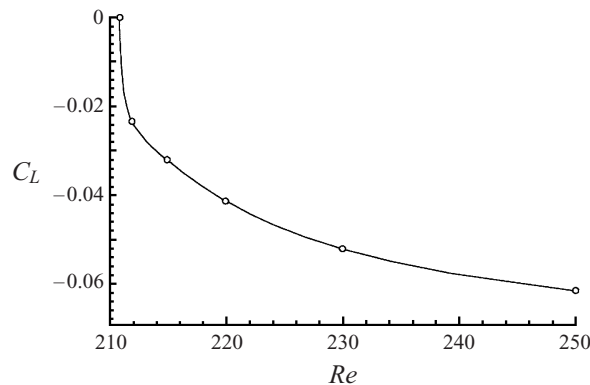
FIGURE 9. Streamlines in a moving reference frame at $Re = 25$.



FIGURE 10. Lateral force coefficient versus Reynolds number, showing loss of axial symmetry.

Dyke's (1982) figure 9, where the photograph is taken in a frame moving with the free stream. This illustrates the advantage of using a quantitative method to reveal vortical structures rather than relying on streamlines, which are reference frame dependent. At higher Reynolds numbers, figures 8(*b*) and 8(*c*) show the thinning of the region adjacent to the sphere's equator and the growth of the toroidal vortex region. The two regions have, in fact, merged at these higher Reynolds numbers.

## 5. Steady non-axisymmetric flow

At a Reynolds number of 211 the calculated flow solution no longer exhibits axial symmetry. The flow does, however, remain steady. The temporal stability of this regime was checked by setting $\Delta t$ in (2) to some finite value and confirming the stability of the resulting solution. Although non-axisymmetric, the flow does contain a plane of symmetry. In the current calculations, the location of the symmetry plane was allowed to arise naturally, forced only by the numerical biases resulting from such things as sweep directions in the solver. Due mainly to the non-physical presence of numerical boundaries in the azimuthal direction, the calculated symmetry plane coincides with the $\eta = \eta_{max}$ plane. Because of the periodic grid overlap, as discussed in §2, the $\eta_{max}$ plane is located 9° off the $(x, y)$-plane. For the purposes of presenting the data, however, the calculated flow field has been rotated such that the symmetry plane coincides with the $(x, y)$-plane.
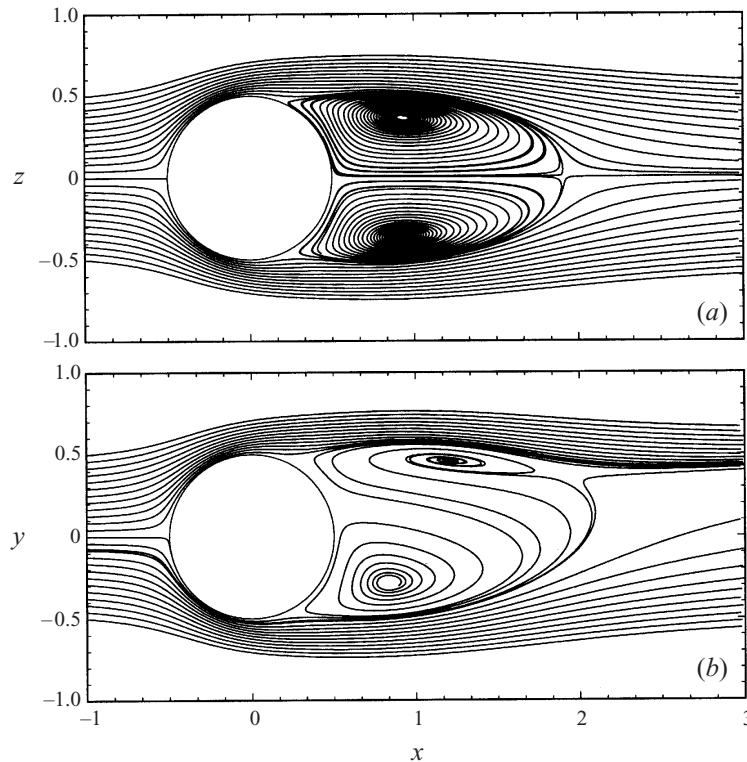
FIGURE 11. Streamlines of projected velocity vectors at $Re = 250$ in ($a$) the $(x, z)$-plane;
($b$) the $(x, y)$-plane.

The onset of the loss of axial symmetry is illustrated in figure 10, which plots the lateral force coefficient $C_L$ against Reynolds number. With the $(x, y)$-plane defining the symmetry plane, the lateral force lies along the $y$-axis and may be denoted as $F_y$. Note that the $y$-axis orientation is arbitrary and that $F_y$ may be positive or negative. For the present orientation $F_y$ is negative. $C_L$ is then defined as $C_L = F_y/(\frac{1}{2}\rho U_\infty^2 \pi D^2/4)$. For axisymmetric flow, $C_L$ is naturally zero. At $Re = 211$, $C_L$ was found to be about $-3 \times (10)^{-5}$ and by $Re = 212$ it had jumped three orders of magnitude to $-2.4 \times (10)^{-2}$.

As discussed in §1, the extent of this steady non-axisymmetric range has been documented experimentally in earlier studies as approximately $210 < Re < 270$ by Magarvey & Bishop (1961), and Nakamura (1976), and numerically by Tomboulides (1993); at $Re > 270$ the flow has been observed to become unsteady. The present results within this regime were found to be essentially self-similar, or topologically identical, and only the solution at $Re = 250$ is considered here since the departure from symmetry is quite pronounced.

The presence of a plane of symmetry in the flow, as mentioned previously, is most obvious in figures 11($a$) and 11($b$), which show streamlines constructed from in-plane velocity vectors in the $(x, z)$- and $(x, y)$-planes, respectively. It is clear from figure 11($a$) that the flow field is symmetric about the $(x, y)$-plane, which divides the figure across the centre. Keep in mind that there are out-of-plane velocity components in figure 11($a$) so that the lines constructed in this manner do not correspond to true three-dimensional streamlines. However, since figure 11($b$) corresponds to the $(x, y)$
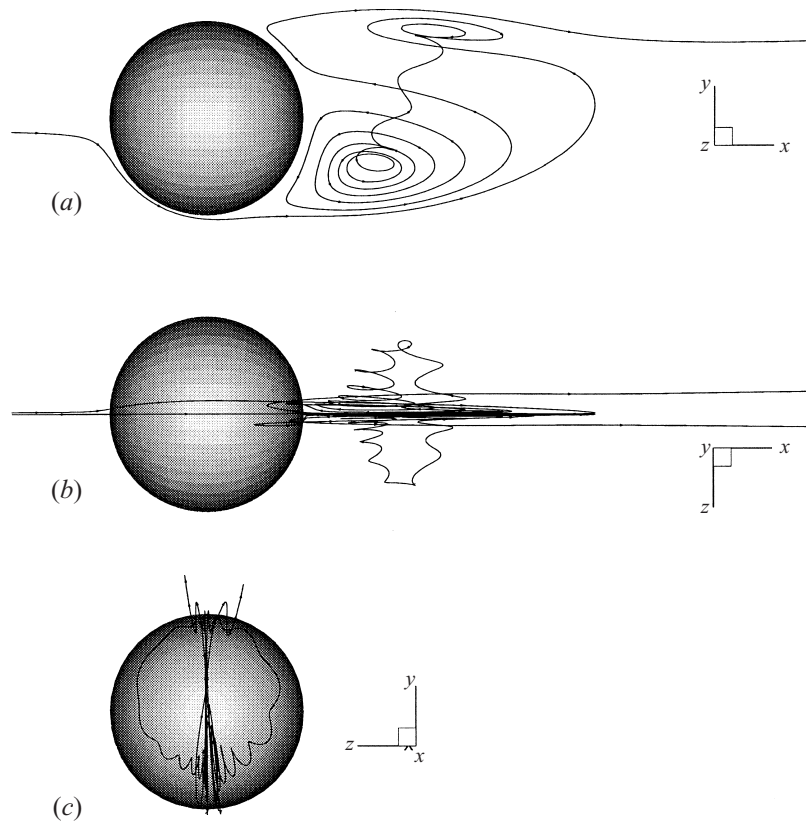
FIGURE 12. A three-dimensional particle path at $Re = 250$:
(*a*) $x, y$ view; (*b*) $x, z$ view; (*c*) $y, z$ view.

symmetry plane, there are no out-of-plane components and the traces do, in this case, represent true streamlines. Considering figure 11(*b*), it is apparent that the toroidal vortex has tilted. It is also clear from the difference between the top and bottom of the vortex ring, that its size is not constant in the azimuthal direction. Additionally, the toroid is clearly no longer a closed separation bubble; the upper spiral is actually fed by fluid originating from upstream while the lower spiral releases fluid into the wake after sending it up and around the upper spiral. Further inspection reveals that, as a consequence of continuity, there must be fluid flowing out from the centre of the upper part of the vortex, and fluid feeding into the centre of the lower part of the vortex. That the flow is, in fact, directly from one to the other via the vortex centres of figure 11(*a*) can be seen in figure 12.

Figure 12 shows $(x, y)$, $(x, z)$ and $(y, z)$ views of the paths of a pair of particles which originate from either side of, and just out of, the $(x, y)$-plane upstream of the sphere. Note that in figure 12(*a*) only one of the two paths is shown for clarity. The traces in these figures show three views of the actual three-dimensional particle path. In figure 12(*a*), the $(x, y)$-projection of the path, it is clear that upstream fluid is entrained into the upper focus of the wake. The pathline spirals clockwise inward then emerges from the centre of the focus and feeds into the centre of the lower focus, where it spirals counterclockwise outward, eventually passing around the upper focus and joining the downstream flow. The directions of rotation of both foci remain consistent with the axisymmetric toroidal vortices at lower Reynolds numbers. In figures 12(*b*) and 12(*c*),
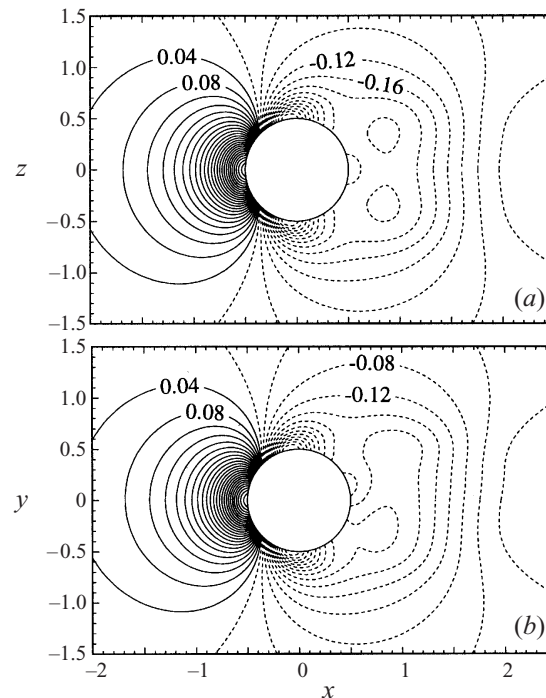
FIGURE 13. Pressure coefficient contours at $Re = 250$: (a) $(x, z)$-plane; (b) $(x, y)$-plane.

the out-of-plane motion and structure of the flow can be seen. These figures show that the flow from one focus centre to the other follows an azimuthal path that coincides with the core of the toroidal vortex. It is also evident in these figures that near-wake fluid is ejected into the downstream flow through two separate streams, one on either side of the $(x, y)$-plane.

Pressure coefficient contours for the $(x, z)$- and $(x, y)$-planes are shown in figure 13. As with figure 6, the contours are drawn in steps of 0.04. The pressure field in the $(x, z)$-plane is completely symmetric and closely resembles the contours in figure 6(d) for a Reynolds number of 200, although the pressure in the core of the vortex is clearly lower owing to the higher centrifugal acceleration of the vortex. Pressure contours in the $(x, y)$-plane are not symmetric. The pressure minimum in the region of the lower focus of figure 11(b) is lower than that in the region of the upper focus: $C_P = -0.252$ vs. $C_P = -0.226$. This azimuthal pressure gradient propagates through the core of the toroidal vortex inducing flow along the vortex axis, as seen in figure 12. This breakdown in axial symmetry, which begins at $Re \approx 211$, corresponds closely with the occurrence of a global pressure minimum in the centre of the vortex. It appears, therefore, that the instability of the axisymmetric flow is connected to the generation, by radial acceleration around the vortex centre, of a ring of low pressure in the wake. An azimuthal pressure disturbance to the ring with a wavenumber of 1 could generate the observed flow through the vortex core. The resultant core flow causes, through continuity, the high-pressure side of the vortex to spiral inward as it serves as the source of the core flow. The low-pressure side of the vortex spirals outward as fluid is fed into its focus. This is observed in figure 12. Furthermore, the radially inward motion of the high-pressure side of the vortex serves as the means for entraining free-stream fluid into the recirculating region and opening up the previously closed separated wake.
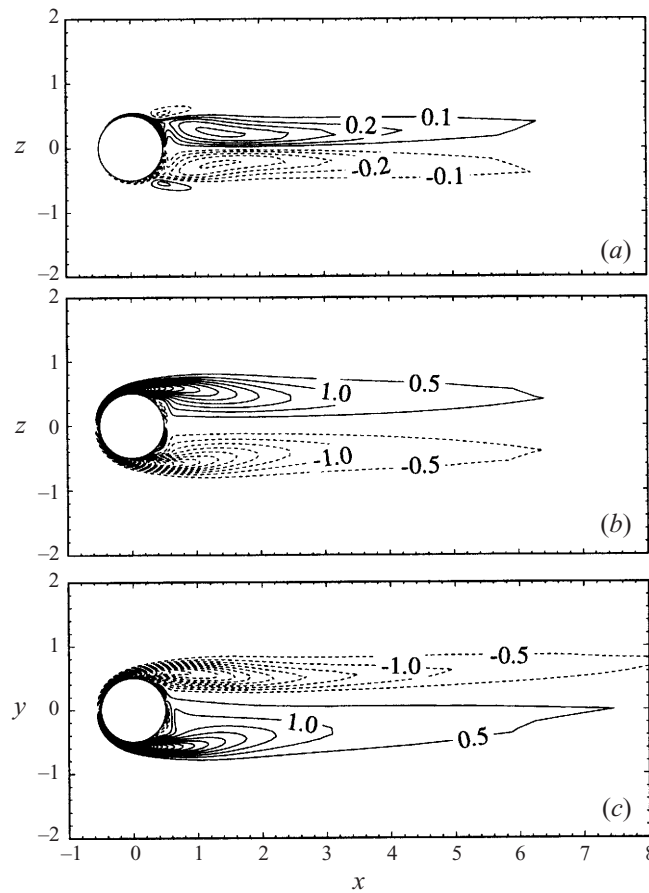
FIGURE 14. Vorticity contours at $Re = 250$: (a) $\omega_x$ in the $(x, z)$-plane; (b) $\omega_y$ in the $(x, z)$-plane; (c) $\omega_z$ in the $(x, y)$-plane.
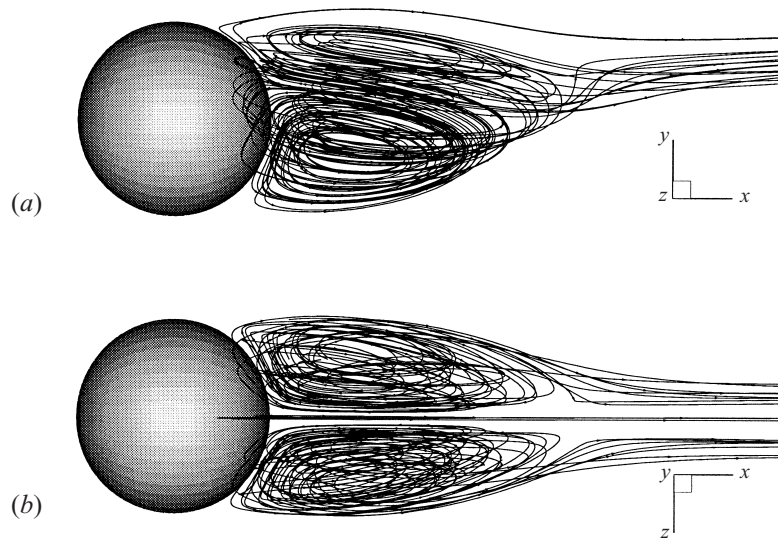


FIGURE 15. Computed three-dimensional particle traces for $Re = 250$, viewed from (a) the $(x, y)$-plane; (b) $(x, z)$-plane.
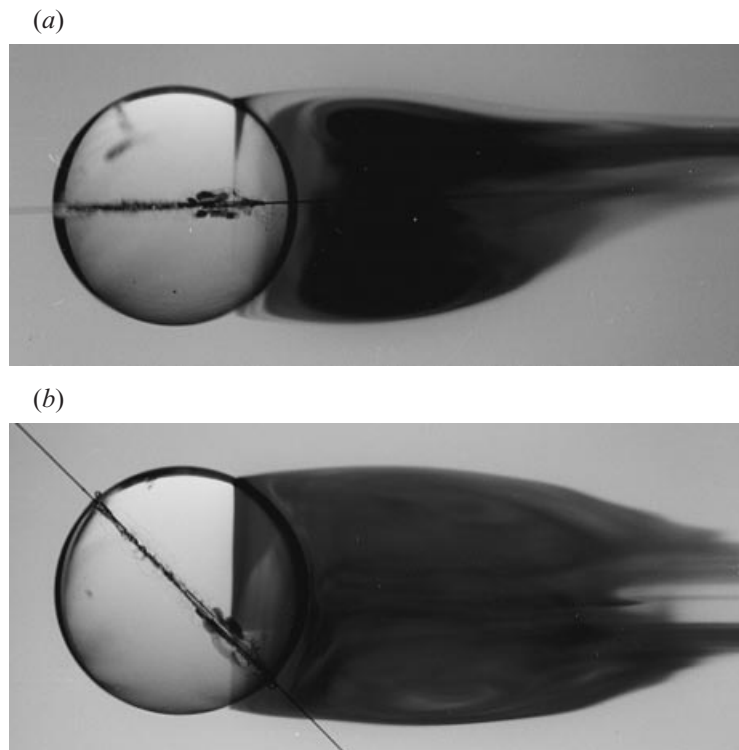
(*a*)

(*b*)

FIGURE 16. Flow visualization results for $Re = 250$: (*a*) $(x, y)$-plane; (*b*) $(x, z)$-plane.

From figure 12(*c*), with the streamwise direction coming out of the page, it is clear that the azimuthal flow will result in the generation of streamwise vorticity. Figure 14(*a*) shows contours of the streamwise vorticity $\omega_x$ in the $(x, z)$-plane. The contours show an antisymmetric distribution of vorticity about the symmetry plane with positive values on the positive-$z$ half of the plane. In figure 12(*c*) the azimuthal velocity in this region is seen to be in a counterclockwise direction. Likewise, in the other half of the plane, the streamwise vorticity is negative, consistent with the clockwise azimuthal flow in figure 12(*c*). Figure 14(*a*) compares well with the isosurface of streamwise vorticity calculated by Tomboulides (1993) at $Re = 250$. Although no mention is made of the particular vorticity magnitude plotted, the form of the surface is the same as the cross-section shown in figure 14(*a*). Contours of $y$-vorticity $\omega_y$ are shown in figure 14(*b*), and of $z$-vorticity $\omega_z$ in figure 14(*c*), in the $(x, z)$- and $(x, y)$-planes, respectively. The contours in the $(x, z)$-plane are symmetric, as expected, and closely resemble those of figure 7(*d*) at a Reynolds number of 200. In figure 14(*c*) the contours are not symmetric and appear to be shifted to the positive-$y$ side of the plane. In addition, the contours on the positive-$y$ side of the plane extend farther downstream than on the negative-$y$ side. Comparison with figure 12(*a*) indicates that fluid escaping the recirculation region is apparently convecting vorticity downstream.

Particle paths showing the escape of fluid from the near wake, as well as the overall geometry of the recirculation region, are given in figure 15, which shows $(x, y)$- and $(x, z)$ views of the three-dimensional paths. Figure 15(*a*) shows the shift of the recirculating fluid to the positive-$y$ side as free-stream fluid is entrained from the negative-$y$ side. In figure 15(*b*) the release of fluid in two separate tails is clearly evident and obviously corresponds to the double-thread wake observed by Magarvey & Bishop
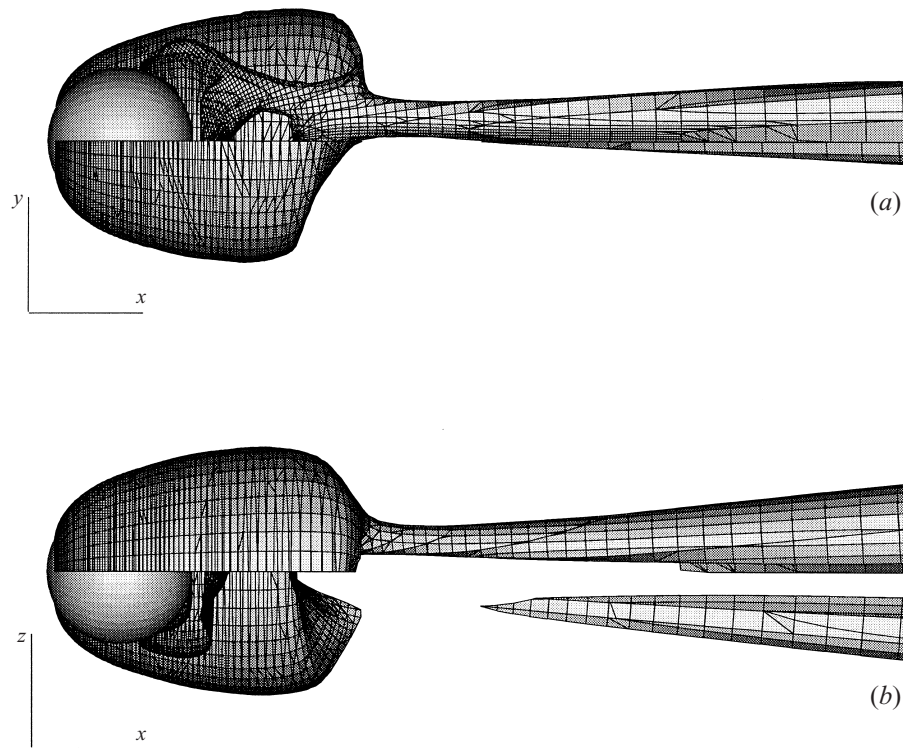
FIGURE 17. Vortical structure at $Re = 250$: (a) $(x, y)$-plane; (b) $(x, z)$-plane.

(1961) for $210 < Re < 270$. These particle traces may be compared with experimental dye visualizations produced in the present study at the same Reynolds number. Figure 16 shows photographs of the dye-filled wake obtained using the method described in §3. The sphere in both photographs is moving to the left, which is equivalent to the flow moving to the right as in figure 15. The support wire lies in the $(x, z)$-plane in both figure 16(a) and figure 16(b). The wire orientation in this case did appear to affect the orientation of the wake. Both figures compare quite well with the particle traces obtained from the numerical solution. The visualizations, just like the numerical results, exhibit a symmetry plane about which are located two tails of dye extending downstream. Furthermore, it is evident that the location and spacing of the dye tails compare quite well with those from the simulations.

While figures 15 and 16 may give some idea as to the general distribution of vortical flow in the wake, the method of Jeong & Hussain as discussed in the previous section has been applied to the numerical results at $Re = 250$ for a more detailed picture. Near-wake $(x, y)$ and $(x, z)$ views of the three-dimensional contour which defines the vortical region are shown in figures 17(a) and 17(b). One quadrant has been cut away to reveal the sphere surface and inner convolutions of the contour. These figures show that the sphere is enveloped in a region similar to that shown in figure 8(c) for $Re = 200$, though shifted with the loss of axial symmetry. Of particular interest are the two trailing vortices extending downstream. These structures extend to the end of the numerical domain. Note that the break in the lower vortical leg in figure 17(b) is due to the removal of one quadrant of the contour. The actual swirling motion indicated by the tails of the contour is evident in streamlines constructed from the $(y, z)$ projected
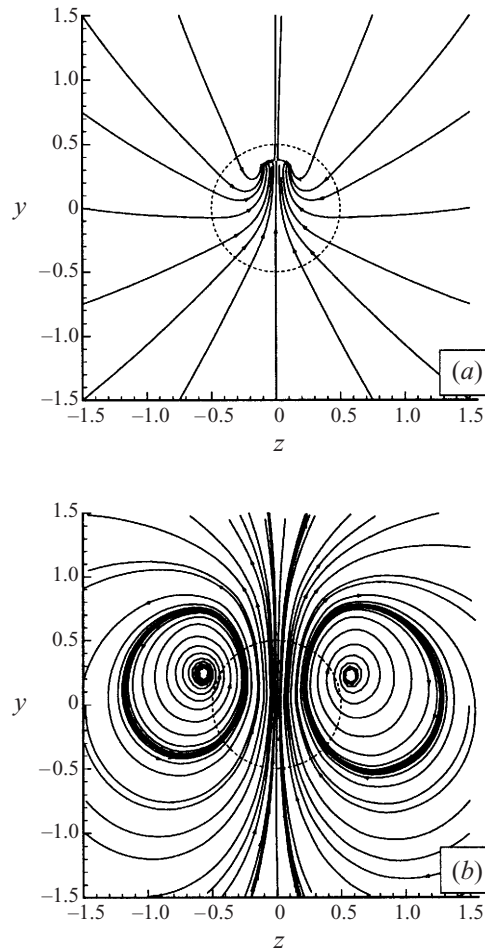
FIGURE 18. Streamlines of the $y, z$ projected velocity vectors of $Re = 250$ at:
(a) $x = 2$; (b) $x = 10$.

velocity vectors, shown in figures 18(a) and 18(b) for constant-$x$ planes at $x = 2$ and $x = 10$, respectively. The extent of the sphere's perimeter is indicated by the dashed circle centred at $(0, 0)$. It is important to remember that these traces ignore the out-of-plane velocity component and therefore tend to exaggerate the spiralling motion of the fluid. Nonetheless, they are useful to reveal the sense of rotation in the wake. Note also that both the spreading and the separating of these trailing vortices are evident and consistent with the contours of figure 17.

## 6. Unsteady flow

The onset of unsteadiness is known from previous studies, both experimental and numerical, to occur at a Reynolds number in the range of 270 to 300. In this work a steady solution was obtained using a finite value of $\Delta t$ in (2) at a Reynolds number of 270. At $Re = 280$, the next highest Reynolds number considered, the solution, which was initialized with the steady non-axisymmetric solution at $Re = 270$, became clearly periodic. No attempt was made to further narrow the range of the onset of unsteadiness since in this transition regime a very large number of iterations was
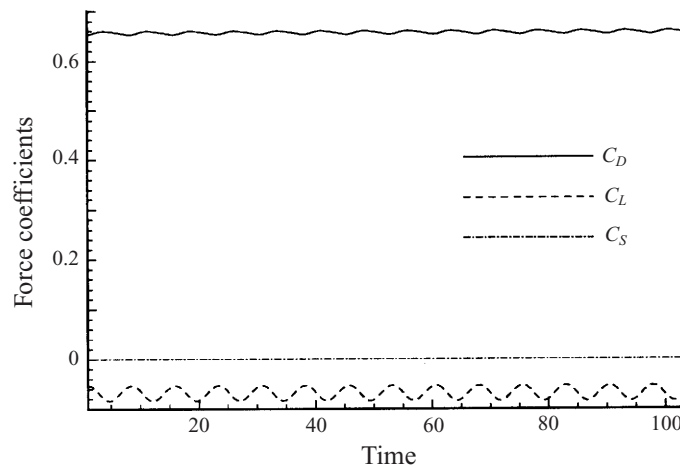
FIGURE 19. Time history of drag, lateral, and side force coefficients at $Re = 300$.

required to damp oscillations en route to a steady solution, when one existed. It should be pointed out that while using the dual-time-stepping approach described in §2, the number of pseudo-time subiterations was restricted for computational efficiency to an allowable maximum of 200. Since the desired convergence may not have been achieved within the maximum number of subiterations, some degree of time accuracy was necessarily sacrificed. This was the case only in the early stages of the calculations, i.e. when the flow from one Reynolds number was used to start the solution procedure at another Reynolds number. Therefore, the transient solution during these impulsive velocity changes was not captured. As discussed in §2, the convergence criterion was to reduce the absolute values of the right-hand sides of (4) and (5), to less than $10^{-5}$. In computing a periodic solution, this convergence criterion was typically satisfied within 20 to 30 subiterations. Obtaining 1000 physical time steps required on the order of 200 hours of Silicon Graphics Power Challenge c.p.u. time, or approximately eight days.

A Reynolds number of 300 was selected as the flow of interest since, while it is solidly in the unsteady regime, it is near enough to the steady flow regime to provide insight into the transition mechanism. The calculation at $Re = 300$ was initialized with the already periodic solution of $Re = 280$. A review of the literature shows measured Strouhal numbers in the range 0.15–0.18 (Sakamoto & Haniu 1990). Based on this expected frequency range, a non-dimensional physical time step of 0.05 was selected to give approximately 120 time steps per period. Numerical experimentation showed this time step to provide satisfactory temporal resolution.

### 6.1. *Force coefficient history*

Figure 19 shows a plot of force coefficients versus time and includes the drag $C_D$ and the lateral and side force coefficients $C_L$ and $C_S$ at a Reynolds number of 300. Here, with the same axis orientation as was used for the steady flows, the side force coefficient $C_S$ is defined for the force normal to the mean flow symmetry plane, i.e. $C_S = F_z/(\frac{1}{2}\rho U_\infty^2 \pi D^2/4)$. Computed average values of $C_D$ and $C_L$ are 0.656 and $-0.069$, with respective oscillation amplitudes of $3.5 \times 10^{-3}$ and $1.6 \times 10^{-2}$. The experimental data of Roos & Willmarth (1971) gives an interpolated value for $C_D$ at $Re = 300$ of 0.629. Tomboulides (1993) found $C_D = 0.671$ with an oscillation amplitude of about $2.8 \times 10^{-3}$. Neither reference reports a value for $C_L$.
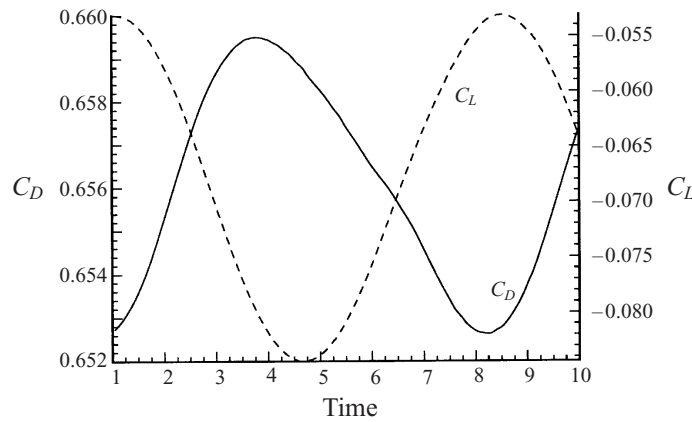
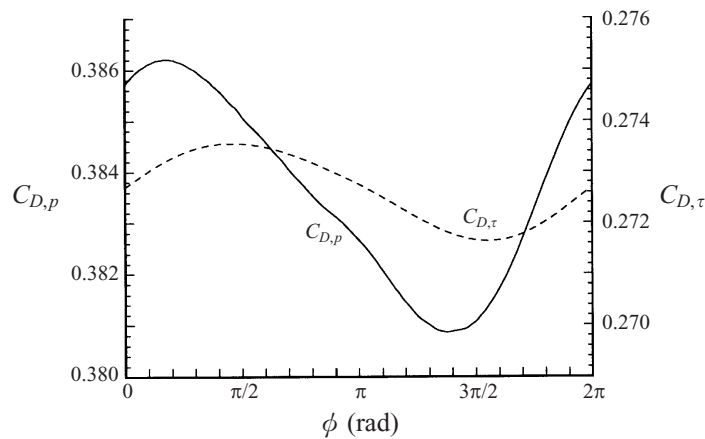FIGURE 20. Expanded view of the time history of the drag and lateral force coefficients.



FIGURE 21. Phase-angle plot of the pressure and friction components of drag.

It is clear from the fact that $C_S$ is always zero that the same $(x, y)$ symmetry that was observed for steady flow is also present in the unsteady flow. In agreement with experimental visualizations, such as those of Achenbach (1974) and Perry & Lim (1978), this symmetry plane remained fixed in time. As was the case for steady non-axisymmetric flow, the symmetry plane was aligned along the $\eta = \eta_{max}$ plane; 9° off the $(x, y)$-plane. Again, for purposes of presenting the data, the flow field has been rotated such that the symmetry plane coincides with the $(x, y)$-plane. The non-zero lateral force coefficient $C_L$, although now oscillatory, is always less than zero, as it was in the steady non-axisymmetric case. This indicates that there is no symmetry, even in a time-averaged sense, across the $(x, z)$-plane.

The frequency spectra for both $C_D$ and $C_L$ contained a dominant peak indicating a Strouhal number of 0.137. This agrees well with the value of 0.136 found by Tomboulides (1993). The experimental results of Sakamoto & Haniu (1990) give a Strouhal number range of 0.15–0.165 at $Re = 300$. Results from the flow-visualization experiments of the current study, obtained by timing shed vortices, gave a range of 0.148–0.165. From the spectra, as well as the plot of figure 19, the magnitude of the lateral force fluctuation was found to be about four times that of the axial force fluctuation. In addition to the Strouhal frequency, there was a second, though much
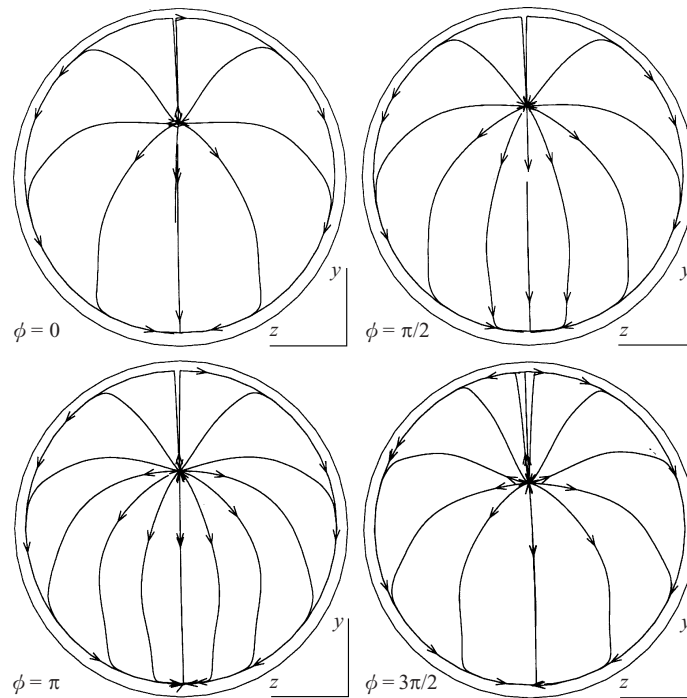
FIGURE 22. Rear surface-limiting streamlines at $Re = 300$ at every quarter period.

smaller, peak in the spectra at twice the Strouhal frequency. This second frequency exhibited a greater effect on $C_D$ than on $C_L$. Figure 20 shows an expanded plot of the force coefficients and, for clarity, covers slightly more than one period of oscillation. Here it is clear that while $C_L$ appears to be a near-single-frequency sinusoid, $C_D$ does not. In addition, $C_D$ appears to contain a small phase lead relative to $C_L$. In figure 21 the drag coefficient is separated into components of pressure drag and friction drag, denoted $C_{D,p}$ and $C_{D,\tau}$. Note that while the increments on both the $C_{D,p}$- and $C_{D,\tau}$-axes are the same magnitude to show relative amplitudes, the ranges are different so that the waveforms are obvious. The pressure drag component is nearly 1.5 times the friction component. This plot shows that the phase lead is due to the pressure component and that the friction drag, like the lateral force coefficient, is more sinusoidal. For this reason, a phase angle $\phi$ is defined based on the waveforms of the lateral force coefficient and the friction drag. The abscissa in figure 21 shows how $\phi$ is defined relative to the drag coefficient components. In figure 20, the $0$–$2\pi$ range for $\phi$ is equivalent to the range $2.8 < t < 9.9$, which corresponds to the (arbitrarily) defined beginning and end of one period of flow. The solution period analysed in this section corresponds to the last complete period shown in figure 19, spanning the non-dimensional time range of about 93 to 100. Naturally, the periodicity of the solution makes this point merely one of passing interest since each period is ideally identical to every other one.

## 6.2. *Near-wake flow*

The topology of the limiting streamlines over the back of the sphere is shown in figure 22. The near-stationary appearance of the limiting streamlines belies the variations observed in the other flow properties. It is clear in this figure that the separation line remains essentially fixed with time. The movement of the rear stagnation point is barely
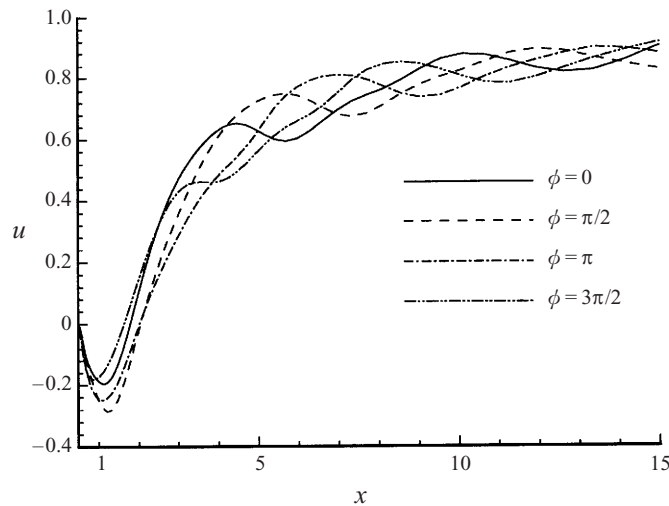
FIGURE 23. Wake axis distribution of streamwise velocity at every quarter period.
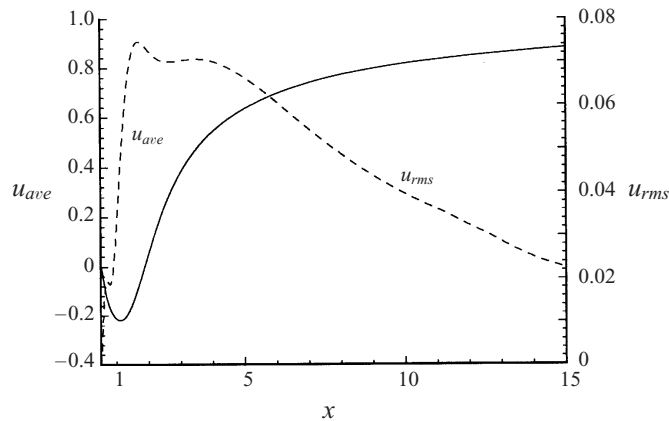


FIGURE 24. Wake axis distribution of average streamwise velocity and r.m.s.

noticeable in this sequence, moving up by just 6° during $\phi = 0$ to $\phi = \pi/2$ then moving down 9° for $\phi = \pi/2$ to $\phi = 3\pi/2$.

Figure 23 shows a plot of the streamwise velocity $u$ along the axis of motion from the rear of the sphere to the end of the solution domain. The distribution indicates the presence of convecting structures in the wake. In particular, a travelling wave moving at roughly $u \approx 0.55$ is indicated: the wave peak at $x = 4.5$ at $\phi = 0$ moves to $x = 8.5$ at $\phi = 3\pi/2$, a time span of 3/4 period, where the period is the inverse of the Strouhal number 0.137. Also of interest is the variation in the reversed flow distance, or the location of zero velocity. This is seen to vary in time from about $x = 1.5$ to $x = 2$, with the largest variation between phase angles $\phi = \pi$ and $\phi = 3\pi/2$, where it drops from $x = 2$ to $x = 1.5$. This is also the phase angle range when the origins of a wave appear in the velocity profile at $x = 3$–4. Figure 24 shows the distribution of the time-averaged velocity along with the r.m.s. distribution $u_{rms}$. The most prominent peak in $u_{rms}$ occurs between $x = 1.5$ and $x = 2$, in the region of flow reversal, with a value of approximately 7.5% of the free-stream velocity. For $x > 4$, $u_{rms}$ begins to decay, as is also apparent in figure 23.

A more global view of the flow may be obtained from pictures of instantaneous streamlines with phase angle. Streamlines constructed from in-plane velocity vectors in the $(x, z)$-plane and the $(x, y)$-symmetry plane are shown in figures 25($a$) and 25($b$) for every quarter phase angle. Note that the region drawn in figure 25 concentrates on the near wake, extending only to $x = 5$; the numerical domain itself extends to $x = 15$. The lines in figure 25($a$), like those in figure 11($a$), are not true streamlines or projections of streamlines, since there exist out-of-plane velocity components. Even more importantly, neither figure represents particle paths since the flow is unsteady. Nonetheless, these streamlines provide a good deal of information about the kinematics of the flow field.

At this point it is important to point out that while the topological features of the wake, the foci, are frequently described below in terms of upper and lower entities, they are in fact just different sections of the same physical structure. The structures remain connected in the azimuthal direction, which means that there are more complicated interactions than the cross-sections in the figures imply. Of critical importance is the fact that when one side of the vortex is said to separate, it remains in some way connected to the lower side, since they are both part of the same vortex ring. The three-dimensional interconnections of the structures in the azimuthal direction will be elucidated in a later section.

Figure 25($a$) shows that the $(x, y)$-plane remains a symmetry plane throughout the period. The movement of the reversed flow region is also clearly evident here. Within the separated flow region the spiral foci undergo interesting changes with time. In the top two pictures, for $\phi = 0$ and $\phi = \pi/2$, the foci are sinks or stable foci, that is, the streamlines spiral in toward the centre. In the bottom two pictures, for $\phi = \pi$ and $\phi = 3\pi/2$, the foci are sources or unstable foci, with the streamlines originating at the centres and spiralling outward. Here the terms 'stable' and 'unstable' do not refer to the stability of the flow, but rather to the topological character of the associated vector velocity field (Tobak & Peake 1982). In stable foci the motion is toward the centre while in the unstable foci the lines spiral outward, indicating a diverging, or unstable, orbit. Keeping in mind that these foci are cross-sections of a three-dimensional vortical structure, it is likely that the stable foci are present during vortex stretching, i.e. the radial fkow is directed inward when there is a positive gradient of axial flow. Likewise, in reverse fashion, the unstable foci could indicate compression, or negative stretching of the vortex axis.

Figure 25($b$) shows the instantaneous streamlines for the same phase angle sequence in the $(x, y)$-symmetry plane. Topologically, at least, the streamlines all resemble those of figure 11($b$), the same cross-section for steady flow at $Re = 250$. At the beginning of the period, in the top panel, there is an unstable focus in the lower half of the near wake corresponding to the lower side of the toroidal vortex at about $x = 0.8$. The line emanating from this focus crosses to the top half of the wake, encircles the top focus, and heads downstream. The top focus, corresponding to the upper side of the toroidal vortex, is located at $x = 1.2$, farther downstream than the lower side. It is also farther from the streamwise axis of the sphere. At its centre, the upper side of the vortex contains an unstable focus enclosed by a limit cycle onto which streamlines converge from both sides. The limit cycle is fed from the outside by fluid entrained from the lower side of the upstream flow. The appearance of this limit cycle in the streamline pattern is most likely due to a shift of the focus from stable to unstable. At the next quarter-phase, the focus on the upper side of the vortex is unstable and the limit cycle is no longer present. The fluid previously entrained now passes around the upper side and ejects into the downstream flow. The focus itself has moved farther downstream
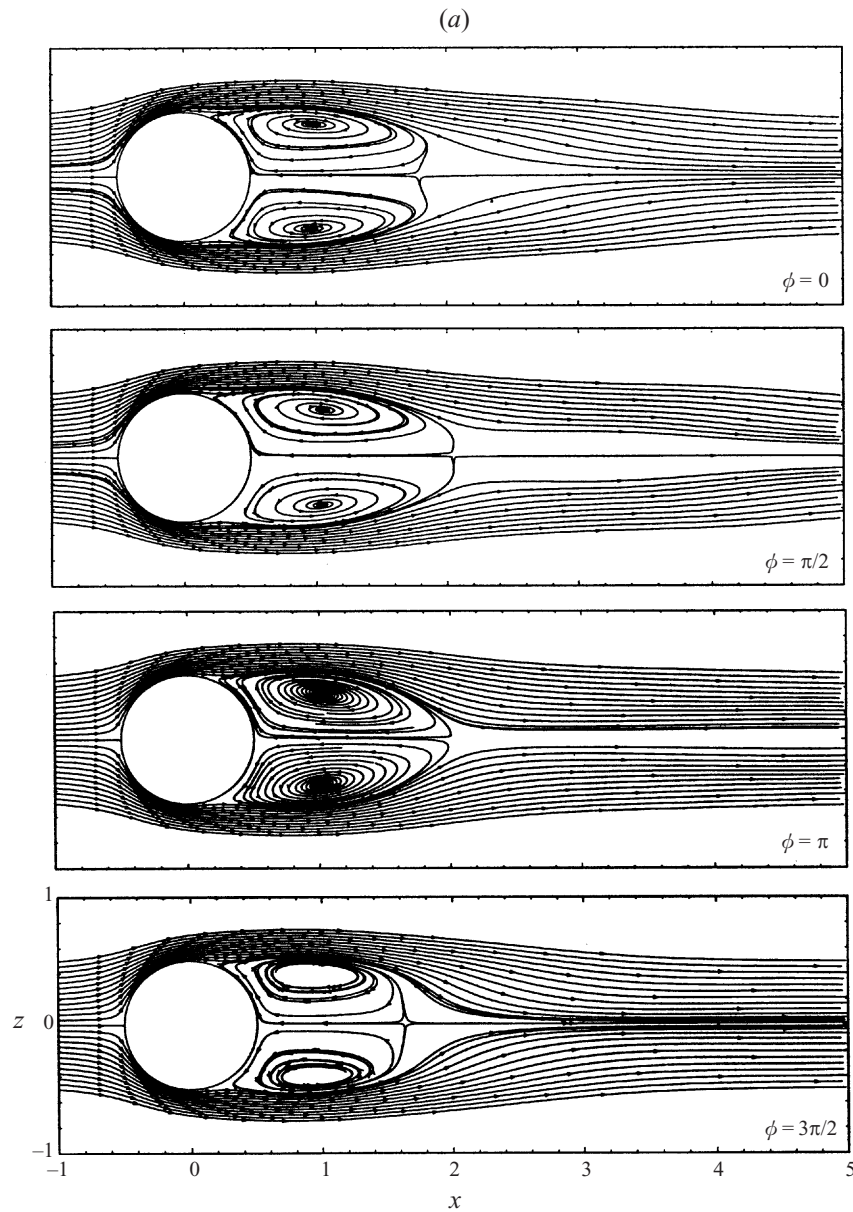
(*a*)



FIGURE 25(*a*). For caption see facing page.

to $x \approx 1.5$. The focus of the lower side of the vortex has changed from unstable to stable, entraining fluid from the lower side of the upstream flow. By $\phi = \pi$, beginning the third quarter of the period, the upper focus is much smaller in size and is located much farther upstream at $x = 0.9$, in line with the lower focus. Indeed, this upper focus is a new feature at this point in the cycle and the previous focus is now convecting downstream having lost its spiral appearance in this reference frame. In other words, the previous vortical structure has broken from the wake, i.e. shed. The new focus is clearly stable and again entrains fluid from the lower side of the upstream flow. The lower focus is unstable and ejects fluid around the upper focus and into the downstream flow. In the final stage of figure 25(*b*) the upper focus has grown
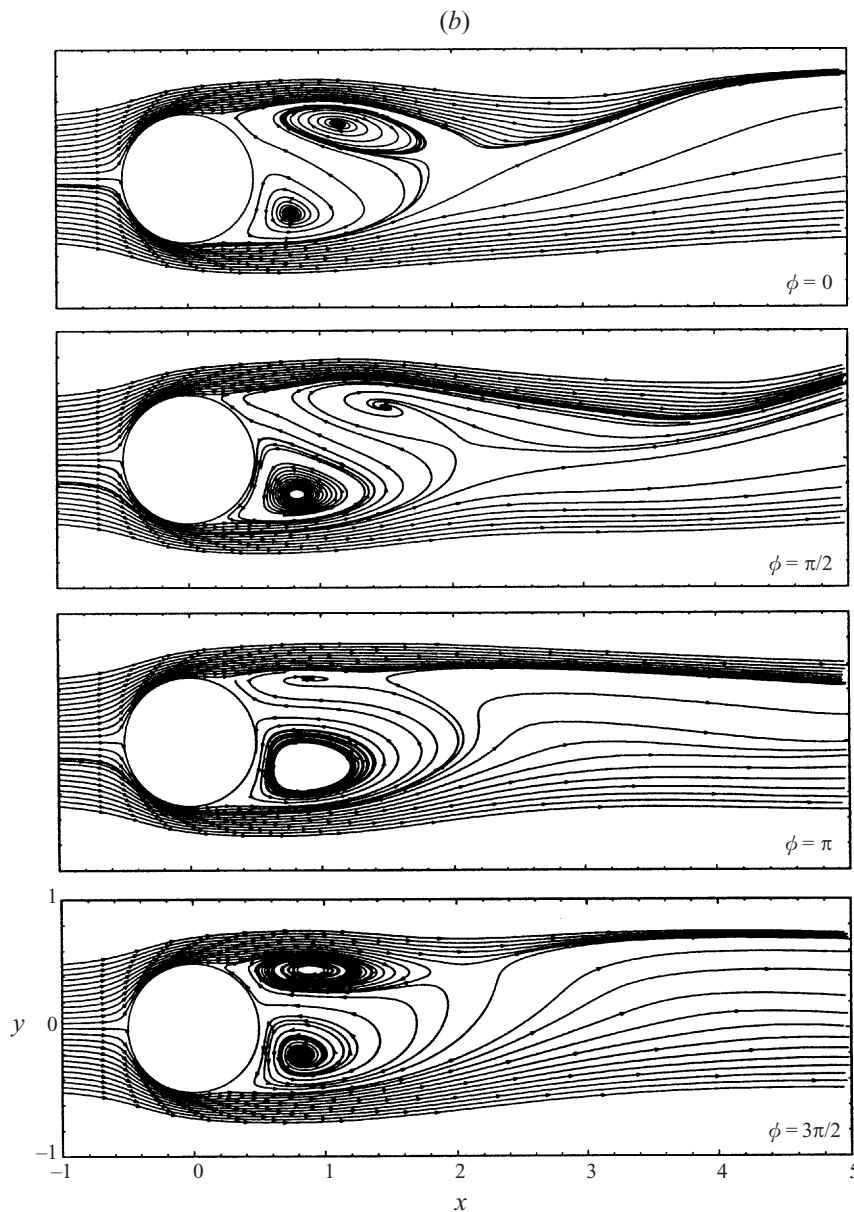
(b)



FIGURE 25. Streamlines of projected velocity vectors at $Re = 300$ for every quarter period:
(a) $(x, z)$-plane; (b) $(x, y)$-plane.

considerably, although it has not moved downstream and remains in line with the lower focus at about $x = 0.9$. Fluid is no longer entrained from the lower side of the sphere. Instead, the upper focus pulls in fluid from the upper side of the sphere as it rapidly grows. To complete the period, the upper focus changes from a stable focus to the unstable focus in the top of the figure. It is clear, then, that the limit cycle surrounding the focus defines the interface of this transition.

Phase series of pressure coefficient contours corresponding to the streamline patterns in figure 25 are shown in figures 26(a) and 26(b). Contours are drawn for every $C_P$ increment of 0.025 with dashed lines to indicate negative values. The contours of figure
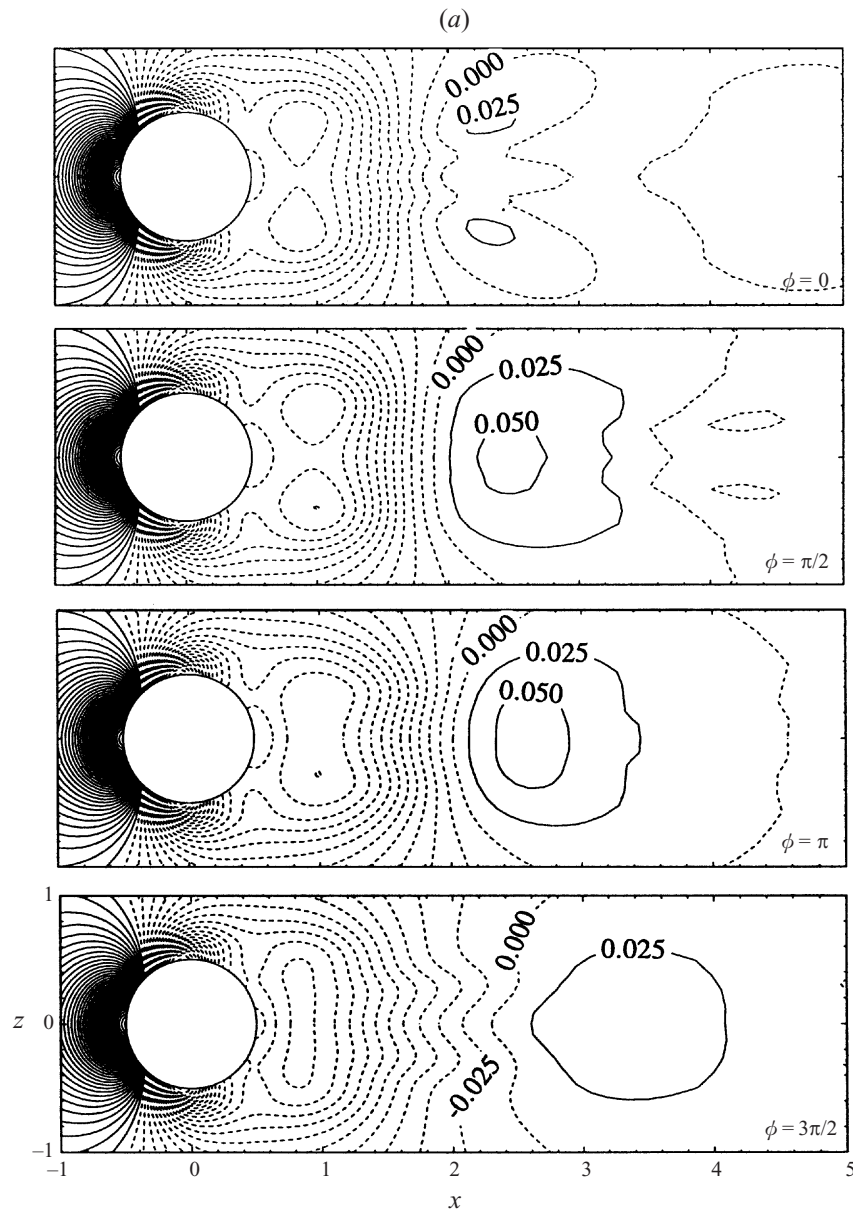
(*a*)



FIGURE 26(*a*). For caption see facing page.

26(*a*) in the $(x, z)$-plane show the symmetry of the flow about the $(x, y)$-plane. In the near wake, the pressure minima at $x = 0.8$–$1.0$ are associated with the foci in figure 25(*a*) and are due to the centrifugal acceleration of the vortical motion. The most noticeable change in the pressure distribution of the near wake is the increase in the pressure at the foci centres at $\phi = 3\pi/2$. Aside from that, the contours give little indication of the periodicity of the flow. Figure 26(*b*) is much more interesting. This shows the $(x, y)$-plane corresponding to figure 25(*b*). Again, the contours are drawn in increments of 0.025. In the first panel of figure 25(*b*), the upper side of the vortex generates a greater pressure minimum than the lower side. The locations of these respective minima are coincident with the centres of rotation, i.e. the foci, seen at the
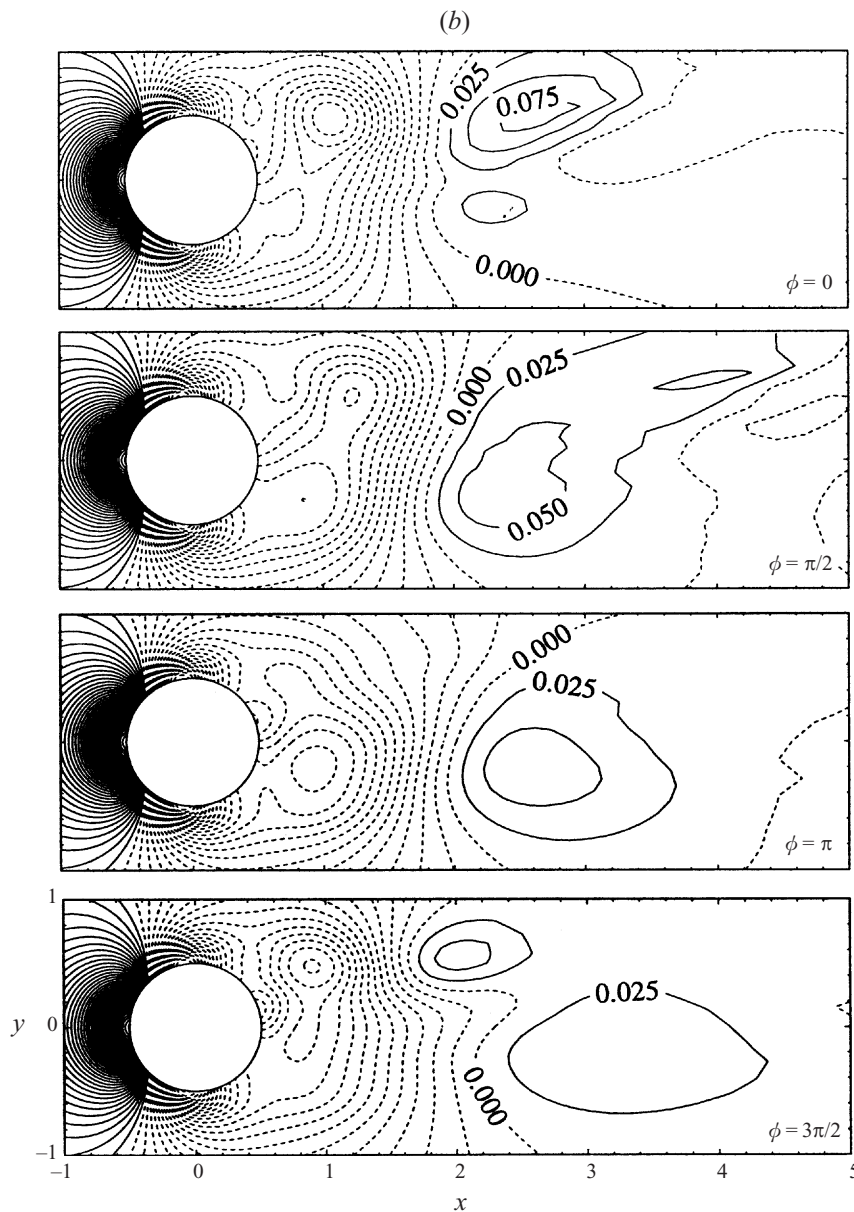
(*b*)



FIGURE 26. Pressure coefficient contours at $Re = 300$ for every quarter period:
(*a*) $(x, z)$-plane; (*b*) $(x, y)$-plane.

top of figure 25(*b*). Just upstream of the upper focus (to the left) and just off the upper-right shoulder of the sphere, at $x \approx 0.5$, is a teardrop-shaped local pressure maximum. In the second panel, at $\phi = \pi/2$, it is now the lower side of the vortex which generates a stronger pressure minimum, while the pressure on the upper side has increased. The local pressure maximum, still upstream of the upper focus, has begun to spread and no longer appears as a closed contour but rather a small region of increased pressure at the top of the near wake. It appears as if this increased pressure is helping to push the upper side of the vortex out of the near wake. In the third stage, the pressure drop associated with the upper focus is no longer evident. The pressure minimum at the

lower focus has intensified and the region of higher pressure has melded into the wake, settling in at $x = 0.8$, corresponding to the location of the new focus in the third panel of figure 25($b$). The new upper focus, then, is formed with a higher core pressure than the lower one. Interestingly, the contours of this phase most resemble those shown in figure 11($b$) for the steady non-axisymmetric case. At the final phase, the last panel in figure 26($b$), the relative strengths of the pressure minima of the opposite sides of the vortex have switched. As opposed to the previous phase, the upper side is now generating a greater pressure drop than the lower side.

### 6.3. *Shedding mechanism*

With the above descriptive account of the instantaneous near-wake flow structures complete, it is now possible to propose a physical mechanism driving the unsteady shedding process. It appears in hindsight that the origin of the phase angle, defined by figure 21, may have best been fixed at $\phi = \pi$, as that serves most naturally as the beginning of the shedding cycle. Also, as the figures for $\phi = \pi$ in figures 25($a$), 25($b$), 26($a$) and 26($b$) are similar to those for the non-axisymmetric steady case in figures 11($a$), 11($b$), 13($a$) and 13($b$), it is convenient to begin a discussion of the process from an understanding of that flow, as described in §4. At this phase, there is an azimuthal pressure gradient set up on the axis of the toroidal vortex in the near wake. This pressure gradient, evidenced by the contours in the third panel of figure 26($b$), generates azimuthal flow from the centre of the upper side of the vortex to the lower side. As was the case for the steady flow, this flow out of the centre of the upper side generates radially inward flow, i.e. a stable focus, which entrains fluid into the wake. In the case of the steady flow, $Re < 270$, this situation attains equilibrium, where the azimuthal pressure-driven flow is sufficiently maintained by the entrainment of fluid into the upper focus. In the current situation, however, the Reynolds number is high enough that the upper focus does not reach an equilibrium state, but continues to grow. As it grows, it begins to entrain fluid from its own side of the sphere, as seen in figure 25($b$). In addition, with the increased intensity of the upper side of the vortex, its centrifugal acceleration sets up a greater radial pressure gradient as seen at the bottom of figure 26($b$).

The cycle continues at the top of figures 25 and 26, with $\phi = 0$. By the time $\phi = 0$, the strength of circulation of the upper focus has increased to the point that it has begun changing from a stable focus to an unstable focus and its radial motion is against its own pressure gradient. As mentioned above, this transition is demarcated by the limit cycle encircling the focus. The increased reversed flow impinging upon the separating flow over the top of the sphere generates the teardrop-shaped local pressure maximum in the top panel of figure 26($b$). The pressure increase appears to push the intensified upper side of the vortex away from the sphere. By $\phi = \pi/2$, the upper side no longer entrains fluid as it continues to move downstream. It was here in the discussion of the instantaneous streamlines that the vortex was said to be shed, though not completely, into the wake. While the upper side of the vortex splits from the near-wake shear layer, the movement of the lower side of the vortex is not clear from the instantaneous streamlines. Finally, following the shedding and subsequent convection of the upper side of the vortex, a strong shear layer is left at the interface of the separated flow and the reversed flow passing through the centre of the wake. This shear layer quickly rolls up to produce the new upper focus in the third panel of figure 25($b$), and with the subsequent growth of this focus the process starts over.

Critical features of the shedding process include the following. First, the unsteadiness is driven by the overshoot of the upper focus past some equilibrium intensity where it

can be balanced by the azimuthal pressure gradient. It can be expected then, that the growth rate of this portion of the vortex dictates the shedding frequency of the wake. Secondly, the shedding of the vortex is facilitated by the strength of the reversed flow it generates and its interference with the separating shear layer. The interference of this secondary cross-flow effectively cuts the vortex out of the wake.

### 6.4. *Vorticity distribution*

To begin further examination of the wake, contours of $\omega_z$ are shown in figure 27 for the $(x, y)$-plane. Contours are drawn for increments of 0.5 with the zero contour omitted for clarity and negative values drawn with dashed lines. The pictures are presented in the same phase angle sequence as earlier figures with $\phi = 0$ at the top. In this first panel, positive vorticity is clearly dominating the region immediately downstream of the sphere. Interestingly, there are no vorticity contours obviously corresponding to the vortical motions observed in the instantaneous streamline patterns. The most notable feature is in the region $2 < x < 3$, where there is a finger of positive vorticity bending upward into the upper half of the wake. In the second panel, which corresponds to the initial shedding of a vortex, the positive vorticity, which was encroaching on the upper half of the wake, has broken down and has, in the process, dissipated some negative vorticity in the region of $x \approx 4$. By the third panel, the negative vorticity looks ready to divide where it interacts with the positive vorticity. At the same time, in the near wake, the positive vorticity has, again, begun encroaching upward across the wake. In the last panel, a segment of negative vorticity has completely broken away from the connected wake vorticity. The positive vorticity in the near wake that had been moving upward is now organizing into what will become the finger-like structure at the top of the figure, poised to split off another segment of negative vorticity. The organized blob of positive vorticity in the lower part of the near wake is clearly moving in reversed flow as it breaks from the rest of the like-signed vorticity. It is apparent that as the upper side of the vortex ring is cut from the near wake and convected downstream, the lower side tears from the wake shear layer and moves deeper into the near wake. This 'tearing' of the lower side of the vortex is similar to the vortex tearing shown recently by Williamson (1996) to be integral in the development of three-dimensional structures in the wake of a circular cylinder. It is interesting that from the vorticity contours a vortex appears to be first shed in the third panel and at a downstream distance of $x \approx 7$, whereas from the instantaneous streamlines a vortex appears to be first shed in the second panel and much closer to the sphere at $x \approx 2$.

Figure 28 shows contours of $\omega_y$ in the $(x, z)$-plane and symmetry once again simplifies the picture. Contours are drawn in the same increments and at the same levels as in figure 27. In the top panel, a segment of vortical fluid has pinched off from each side of the connected vortical fluid in the wake. In the second and third panels additional contour levels have been added to help track the movement of the separated vorticity as it dissipates. By the last panel the separated vorticity has moved out of view. Meanwhile, two more segments are preparing to split away, revealed by another additional contour level placed within the region of connected vorticity.

Figure 29 shows contours of streamwise vorticity $\omega_x$ in the $(x, z)$-plane. These contours are drawn in intervals of 0.05, and are an order magnitude smaller than the $\omega_y$ values of the previous figure. The distribution is antisymmetric across the $(x, y)$-plane and alternates sign in the streamwise direction. It is easiest to follow the evolution of the streamwise vorticity by starting at the third panel in the series for $\phi = \pi$. In the near wake, adjacent to the rear of the sphere, the streamwise vorticity is
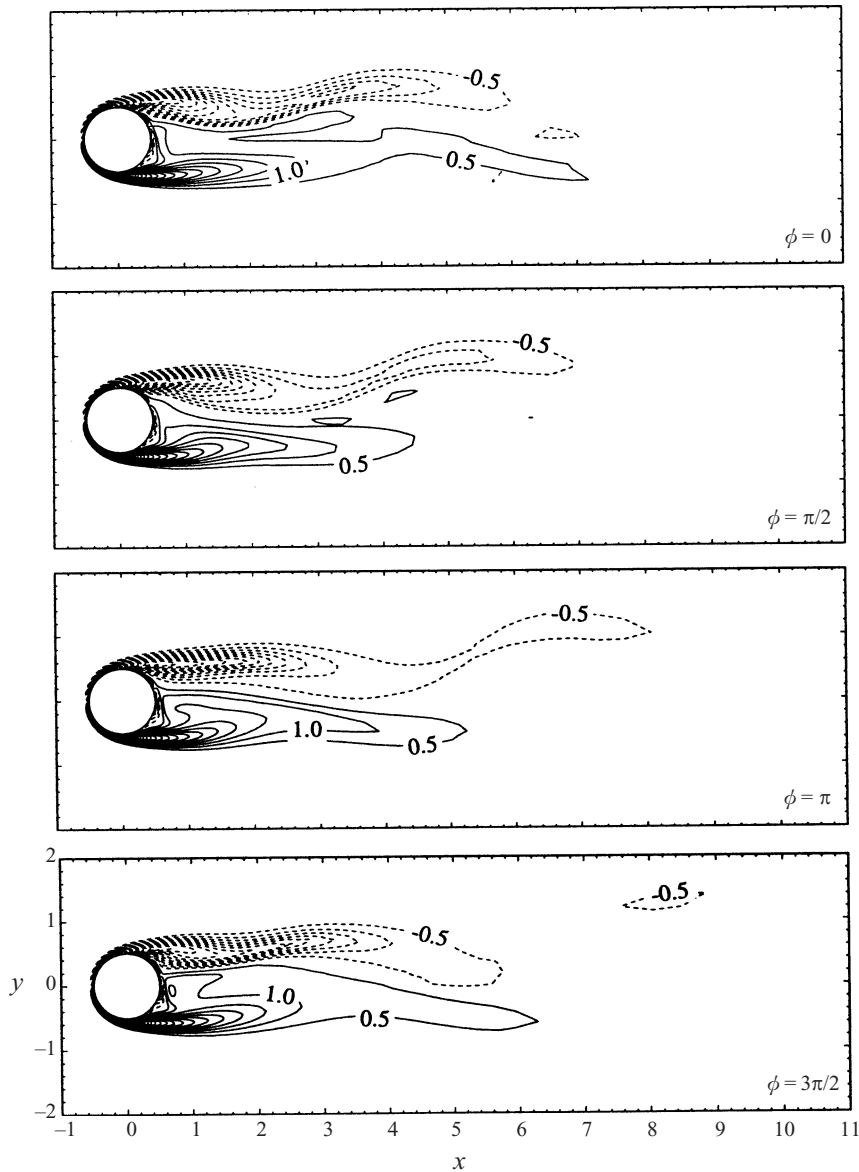
FIGURE 27. Contours of $\omega_z$ at $Re = 300$ for every quarter period in the $(x, y)$-plane.

positive for $z > 0$ and negative for $z < 0$. These signs of streamwise vorticity indicate an induced velocity in the region between them directed into the page. Above the positive vorticity and below the negative vorticity of the inner wake are, respectively, regions of negative and positive vorticity between the wake flow and the generally inviscid outer flow. Similar interactions are evident in figure 14(*a*) which shows analogous contours of counter-rotating vorticity for the steady case. In the fourth panel the inner-wake vorticity has stretched out considerably with the surrounding counter-rotating vorticity following. Continuing the sequence to the top of the figure, the inner-wake vorticity has split and enveloped the counter-rotating vorticity, resulting in the necking down of the inner-wake vorticity in the region near $x = 1.5$ and the formation of outward extended lobes of inner-wake vorticity near $x = 1$. In the
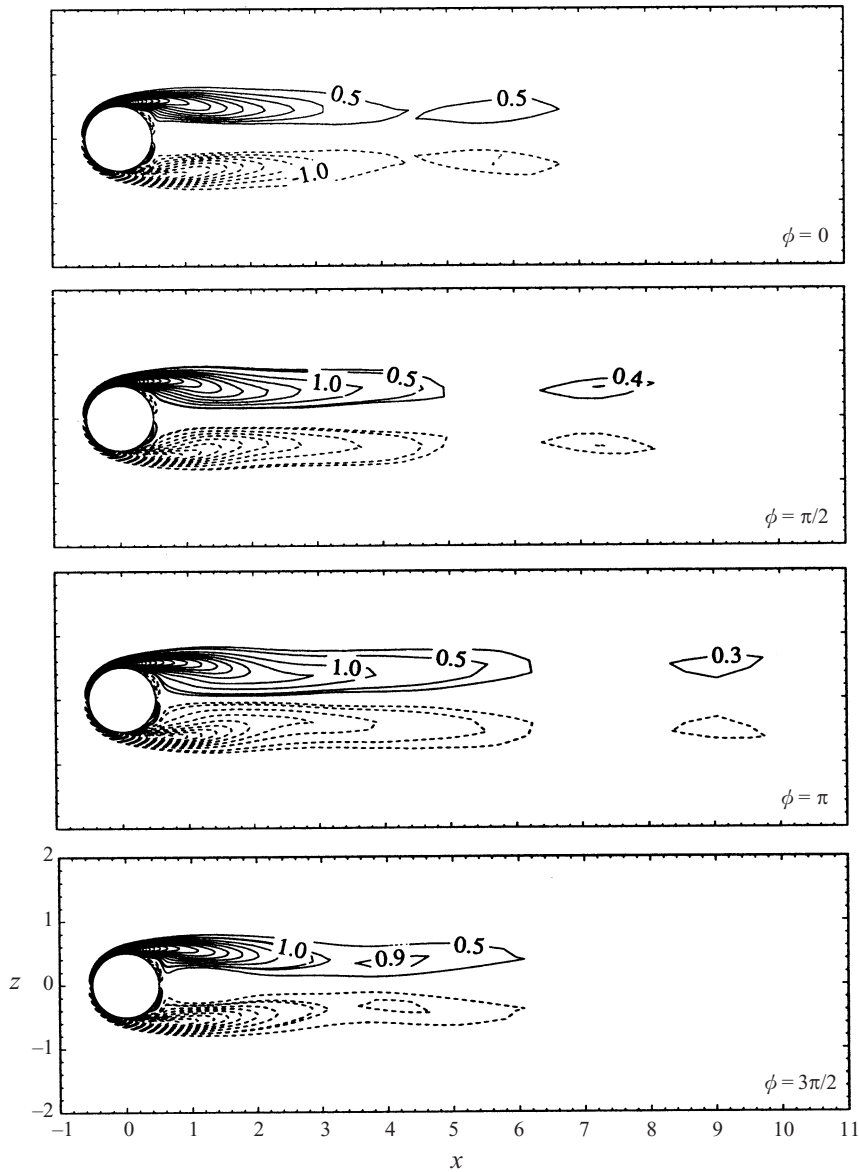
FIGURE 28. Contours of $\omega_y$ at $Re = 300$ for every quarter period in the $(x, y)$-plane.

second panel the enveloped counter-rotating vorticity has further stretched the inner-wake vorticity and the extending lobes have grown considerably. To complete the cycle, in the third panel, the enveloped vorticity has completely split what was the inner-wake vorticity and the growing lobes of inner-wake vorticity are set to restart the cycle. Notice that throughout the cycle, the sign of the streamwise vorticity immediately adjacent to the rear surface of the sphere, the inner-wake vorticity, remains the same and the alternating sign of the vorticity in the downstream wake is due to the envelopment of the oppositely signed counter-rotating vorticity.

The streamwise contours in figure 29 can be compared to the isosurface of streamwise vorticity shown by Tomboulides, Orszag & Karniadakis (1993) at $Re = 300$ in their figure 7. The vorticity magnitude of their isosurface is not known but the sign
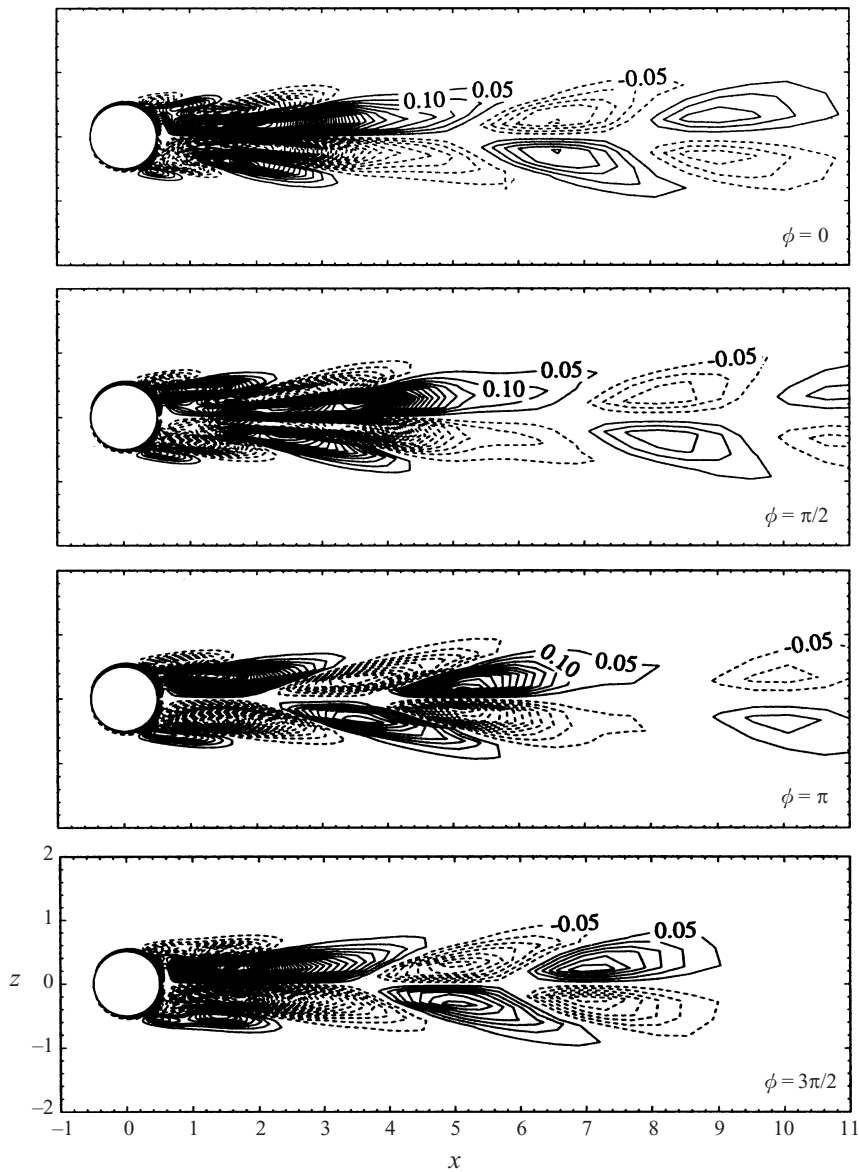
FIGURE 29. Contours of $\omega_x$ at $Re = 300$ for every quarter period in the $(x, z)$-plane.

of the vorticity agrees with figure 29 and the overall form of the alternately shed vorticity is quite similar. Indeed, the streamwise extent of the discrete vorticity sections can be approximately measured as three diameters in both figures. This favourable comparison is not surprising given the previously noted similarity in calculated Strouhal numbers: 0.137 in the present case and 0.136 in Tomboulides (1993).

### 6.5. *Vortical structure*

As was the case with the steady flow results, the streamlines and vorticity contours fall short of providing a clear picture of the vortical structure of the wake. Therefore, the method of Jeong & Hussain (1995), briefly described in §4, has been employed to reveal the regions of vortical motion. Recall that their method defines a vortex core as a

connected region containing two negative eigenvalues of $\boldsymbol{S}^2 + \boldsymbol{\Omega}^2$, where $\boldsymbol{S}$ and $\boldsymbol{\Omega}$ are the rate of strain and the rate of rotation tensors, respectively. This approach essentially demarcates regions in the flow field where swirling motions contribute to the generation of local pressure minima. The results of the method applied to the current flow are shown in figures 30($a$) and 30($b$) for the $(x, z)$-plane and the $(x, y)$-plane. In addition, figure 31 shows an oblique view of the same contour for each of the four phase angles. These oblique views help convey the three-dimensional form of the vortical structures and clearly reveal the hairpin structure of the shed vortices.

The shedding process in figure 30, as with previous figures, begins in the third panels of the figures at $\phi = \pi$. Here, a vortex has just been shed from the previous cycle, though it is seen as still attached to the coherent structure enveloping the sphere. The vortex is clearly in the process of breaking away, as indicated by the folds in the surface of the structure. This phase is shown obliquely in figure 31($c$), which provides a good view of the folding occurring with the separating vortex. In the third panel of figure 30($b$) the head of the nascent hairpin is visible and beginning to extend downstream. At this point, it is known from the earlier analysis that a new vortex is just beginning to form, embedded in the structure just upstream of the emerging hairpin. In the bottom panel of figure 30($a$) the head of the shed hairpin is now about three diameters downstream of the sphere centre and its legs extend directly into the near wake. In figure 31($d$) the extension of the legs into the near-wake region is even more apparent. It is now evident from figures 30($a$) and 30($b$) that the streamwise vorticity contours of figure 29 capture the $(x, z)$-cross-section of the legs of the hairpin vortices. Furthermore, the $\omega_z$ contours in figure 27 reveal the link between the legs within the near wake. The segment of positive vorticity in the last panel of figure 27 located immediately behind the sphere is the link connecting the ends of the vortex legs, i.e. the upstream bight of the vortex ring.

In the top panels of figures 30($a$) and 30($b$), the hairpin vortex has continued convecting downstream and a new vortical structure is developing around the legs of the hairpin. Figure 31($a$) corresponds to this phase and also shows the development of this new vortical structure. Comparison with figure 29 suggests that this structure is a result of the vorticity induced by the wake/outer flow interaction. From figure 31($a$) it is apparent that this structure is forming primarily along the sides of the sphere immediately adjacent to the legs of the hairpin. The top panel of figure 27 shows that the vorticity of the upstream bight is flattening out and beginning to dissipate. In the second panels of figures 30($a$) and 30($b$), the induced outer-flow structure has extended downstream, in agreement with figure 29, and now includes a free-floating structure on the negative-$y$ side of the hairpin vortex. The shape of this structure is particularly clear in figure 31($b$) where it is evidently the head of a developing hairpin. Obviously, this is not a monopole of vorticity, but is most probably a previously unrevealed continuation of the induced structure, which earlier in the shedding process had not been intense enough to show up using Jeong & Hussain's method. Also in the second panel of figure 30($a$) the sphere-enveloping structure has begun to show the folding that preceded the total release of the shed vortex. In figure 30($b$) the enveloping structure shows a hole on the top. This hole is due to the non-vortical fluid which enters the bottom of the wake region and passes out through the top in the third panel of figure 25($b$). This is the initial break in the shedding vortex's connection to the near wake. In the next panel, the hole has been filled in by the shear-layer-generated vorticity and the brand new focus. This cycle repeats and figure 30 reveals the alternating presence of wake-shed hairpin vortices, which are always oriented up in figure 30($b$), and the hairpin vortices induced by the interaction of the wake flow with
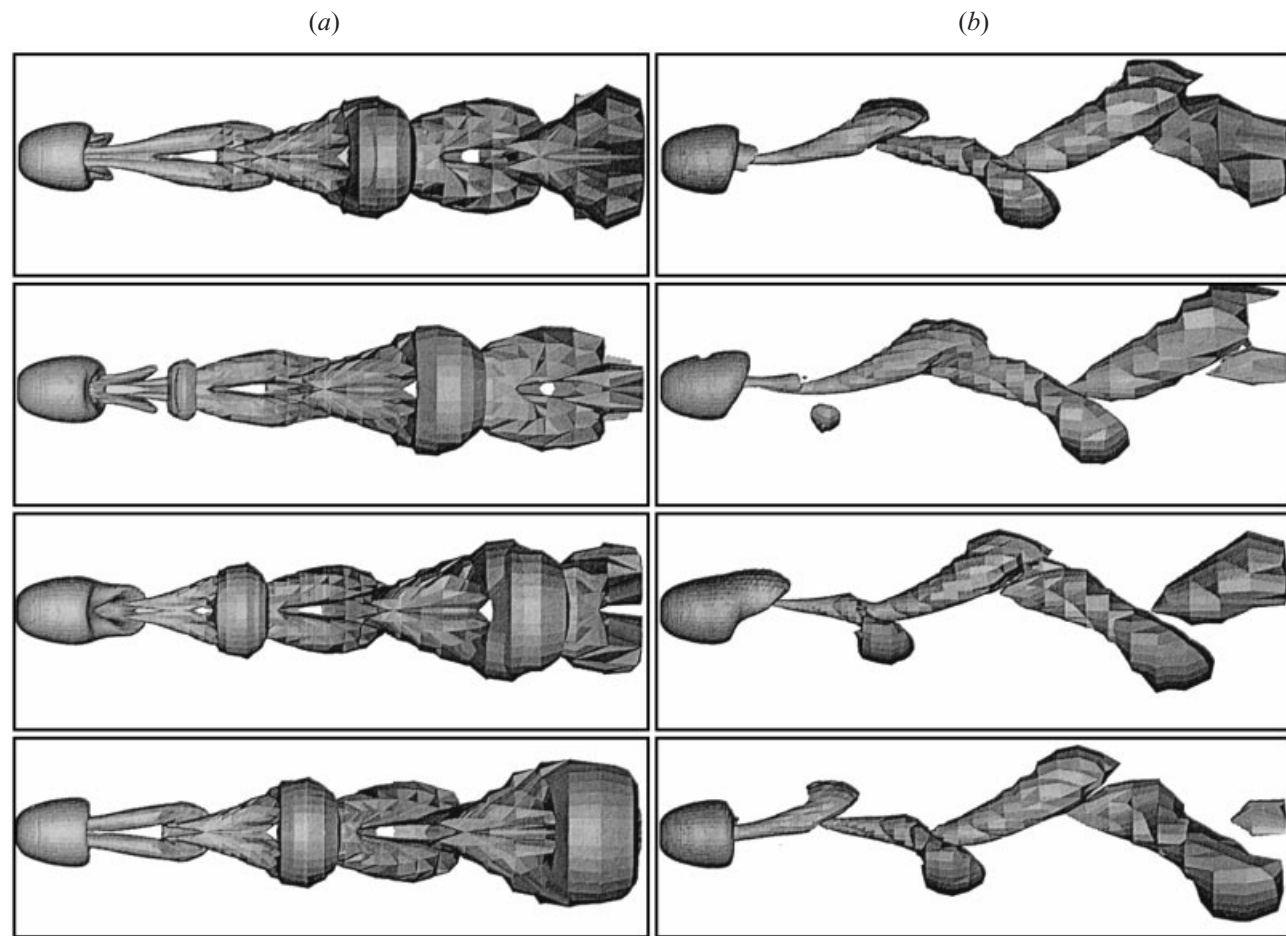
(a)    (b)

FIGURE 30. Vortical structure at $Re = 300$ at every quarter period: (a) $x, z$ view; (b) $x, y$ view.
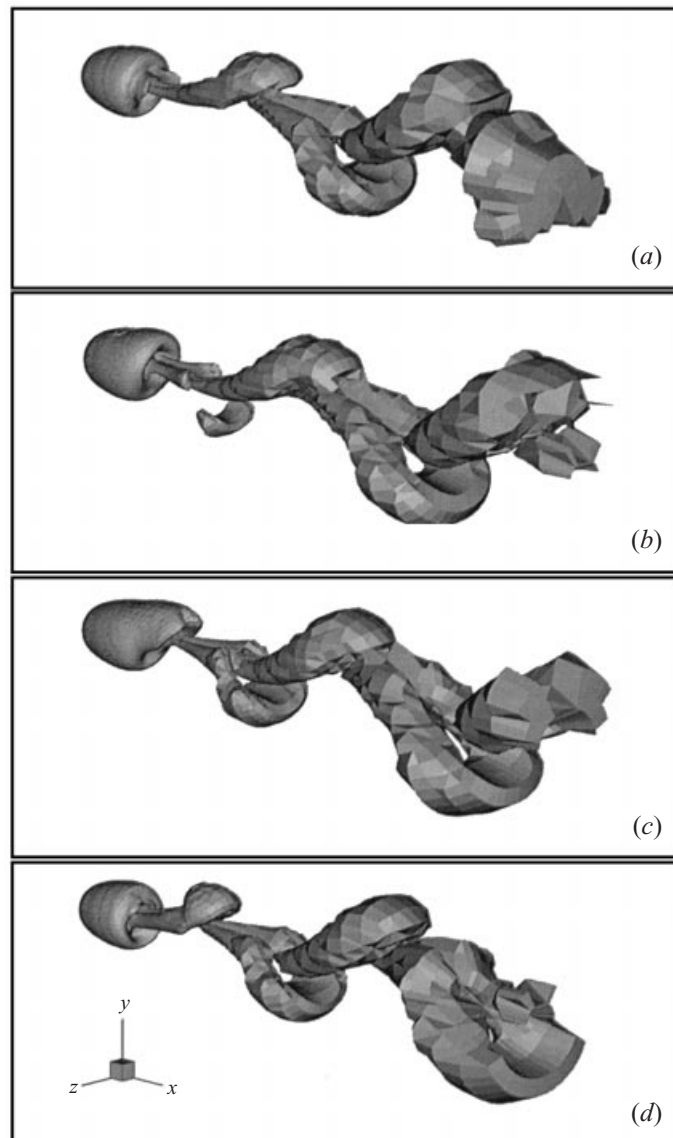
FIGURE 31. Oblique views of the vortical structure: (a) $\phi = 0$; (b) $\phi = \pi/2$;
(c) $\phi = \pi$; (d) $\phi = 3\pi/2$.

the outer flow, which always point down in figure 30(b). Recalling figure 29, it is seen that the wake-shed hairpins, which have $\omega_x > 0$ above the x-axis and $\omega_x < 0$ below, always originate from within the inner wake. The induced hairpins, which have the opposite $\omega_x$ sign, originate in an area surrounding the central wake and are folded into the wake, perhaps by the induced velocity of the separating shear layer surrounding the wake.

Since the surface of the sphere and the near-wake region are completely covered by vortical flow, cross-sections of the structures are presented in figure 32(a–d). These figures are ordered beginning with $\phi = \pi$, since that was determined above as the most logical starting point for the shedding process. These figures show cross-sections in the (x, y)- and (x, z)-planes with the (x, y)-plane on the left side of the figure. The (x, y)-
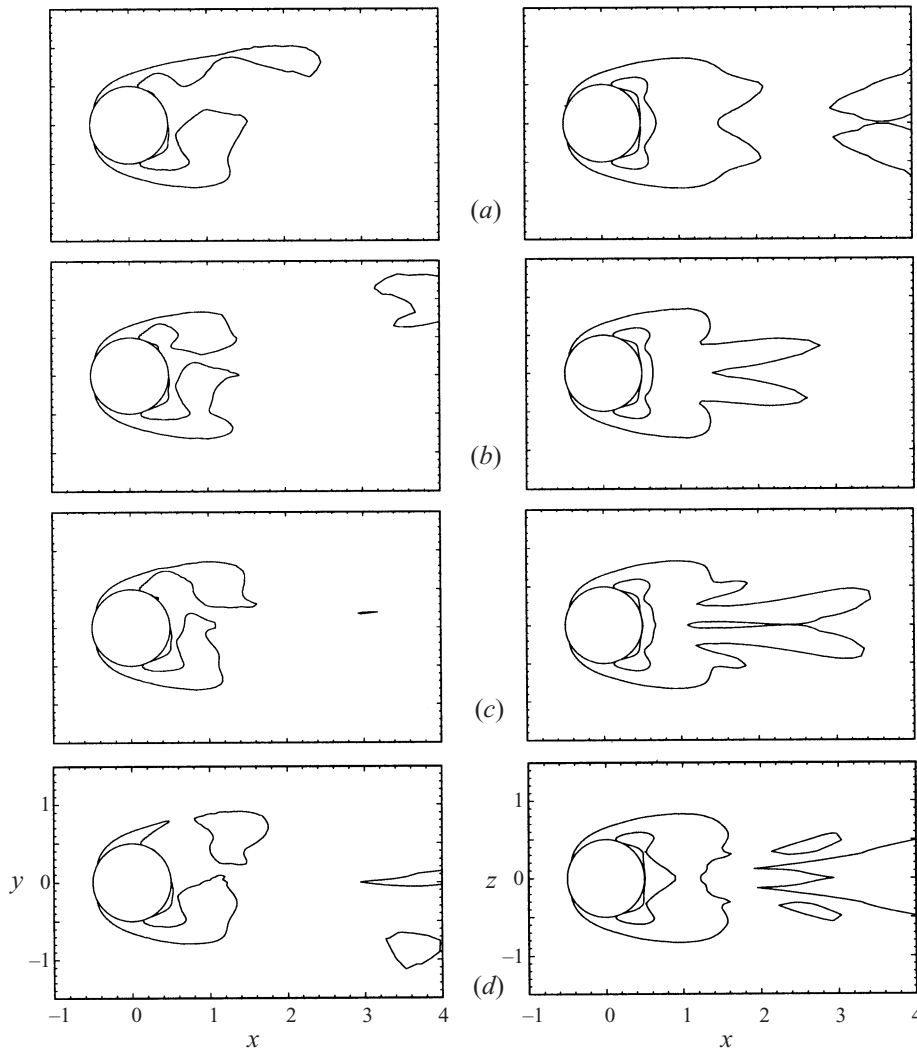
FIGURE 32. Slices of the vortical region at $Re = 300$ in the $(x, y)$ (left) and $(x, z)$ (right) planes:
(a) $\phi = \pi$; (b) $\phi = 3\pi/2$; (c) $\phi = 0$; (d) $\phi = \pi/2$.

plane of figure 32(a) shows that the vortical region is generated in a cylindrical sheath surrounding the near wake. The separating vortex is located on the upper side of the wake at $x = 2$ and the new shear-layer vortex is located at $x = 0.8$. Immediately downstream of the sphere is a large region which makes up the lower portion of the separating vortex. In the $(x, z)$-plane the inclined sides of the separating vortex can be seen protruding from the rest of the region which constitutes the lower bight of the separating vortex. In the $(x, y)$-plane at the top of figure 32(b), which corresponds to $\phi = 3\pi/2$, the head of the separated vortex has nearly moved out of the picture while the other end of the ring has moved nearer to the sphere. Meanwhile the new vortex has grown substantially. In the $(x, z)$-plane in the lower half of the figure, the legs of the hairpin vortex are now even more distinct. The vortical region in the $(x, y)$-plane of figure 32(c) has changed only slightly from the previous phase angle. The near-wake bight of the separated vortex appears to have contracted and the upper region shows a small protrusion on the downstream edge. With reference to figure 30(b), this
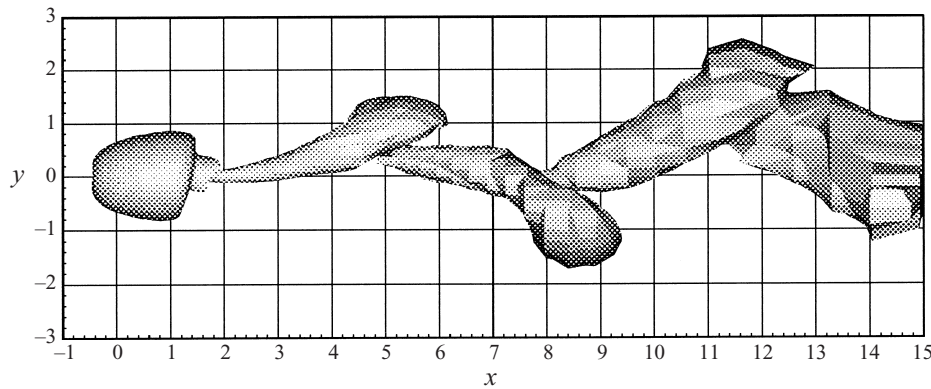
FIGURE 33. Grid-overlaid view of the vortical structure at $Re = 300$ in the $(x, y)$-plane.

protrusion corresponds to the region of induced vortical motion just beginning to form around the legs of the hairpin in the top panel of the figure. In the $(x, z)$-plane of figure 32(c), along with the legs of the hairpin, the induced vortical region is even more pronounced than in the $(x, y)$-plane. Figure 32(d) completes the cycle and shows, quite clearly, the break of the vortex from the rest of the structure. At the lower right of the $(x, y)$-plane, at about $x = 3.5$, the free floating head of the induced hairpin is visible. Just above is the intersection of the legs of the previously separated vortex with the $(x, y)$-plane. The breaks in the vortex legs in the $(x, z)$-plane in figure 32(d) are due to movement of the structures out of this plane. Close inspection of the second panels of figure 30 shows that the legs of the induced hairpin remain intact. The legs of the previously shed hairpin do, however, taper away.

This dissection of the near-wake vortical region shows that the structure remains hollow throughout the cycle This is to be expected since interaction between opposing vorticities across the centre of the wake results in their mutual dissipation. Also evident from the cross-sections is that, for whatever reason (most likely the intensity of the vortex), the upstream end of the vortex ring never appears to strongly interact with the surface of the sphere, leaving the limiting streamline topology relatively unaffected as shown in figure 22.

With the vortical regions, as defined by Jeong & Hussain's method, thoroughly analysed, it remains to translate the meaning of these structures into fundamental flow properties. This is best accomplished by looking at cross-sections of the structures in planes of constant $x$. Figure 33 shows the vortical region that was calculated at $\phi = 0$. It has been plotted over a numbered grid to help illustrate the positions of the cross-flow planes being considered relative to the vortical structure. It is important to remember that the structure does not strictly define the extent of the vortical region of the flow. As indicated by the appearance of a free-floating structure in the second panels of figures 30(a) and 30(b), the method merely sets a threshold for structure definition. Clearly then, there is a limit to the details which can be extracted from these structures and care is taken such that the following analysis does not exceed this limit.

In the region of $x \approx 1.5$ there is a structure developing around the legs of the hairpin vortex. Previously it was concluded, from a comparison with figure 29, that this structure is a result of the vorticity induced by the wake/outer flow interaction. To clarify this, figure 34 shows a $(y, z)$-plane taken at $x = 1.5$. Exploiting the symmetry of the flow field, the figure is split into two halves. The left half shows the cross-section of the vortical structure. The right half shows cross-flow velocity vector traces, which
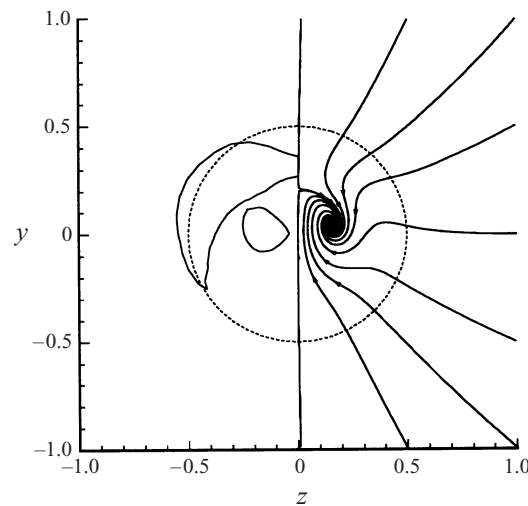
FIGURE 34. Combination plot of the cross-section of the vortical structure and integrated traces of cross-flow vectors at $x = 1.5$.

are simply streamlines constructed from the in-plane velocity vectors. The projected perimeter of the sphere is shown as a dashed outline. The most prominent feature of the streamlines is the clockwise rotating focus at $y = 0$, $z = 0.2$. On the left side of the figure this structure is captured by a circular contour line. With reference to figures 31, $30(a)$, and $30(b)$ this focus is obviously one of the legs of the shedding hairpin vortex. The other contour, somewhat banana shaped, and sitting above and to the left of the hairpin leg, clearly corresponds to the induced vortical structure. Considering the region of the streamlines that would be covered by reflecting the contour section about the centreline, the mechanism behind the generation of this vortical region becomes clear. As the far-field flow approaches the rotating vortex of the hairpin leg, it gets turned sharply as it is dragged into the vortex. Unlike the hairpin leg, which is spinning clockwise, the induced motion of the outer flow is counterclockwise. Note that even though the curvature of the induced flow does not appear to indicate the presence of a vortex, it is nevertheless sufficient to register as a structure using Jeong & Hussain's method.

Cross-flow velocity vector traces have been generated farther downstream in the wake in order to reveal more about the hairpin vortex structures. One sequence of planes has been taken for $4 \leqslant x \leqslant 6$ to provide information on the flow behaviour in the region of the hairpin vortex's head and the induced hairpin's tails. Another sequence has been taken for $7.5 \leqslant x \leqslant 9$ to reveal the behaviour in the opposite situation, passing through the induced vortex's head and into the next hairpin's tails.

The first cross-flow sequence is shown in figure 35 and includes planes at $x = 4$, 5, 5.5 and 6. Note that the axis range has been changed relative to figure 34 and that the profile of the sphere is still indicated by a dashed circle. With reference to figure 33, this sequence spans from just upstream of the hairpin's head to the legs of the downstream induced hairpin. Figure 35 is organized in the same manner as figure 34, with vector traces on the right and contours on the left. In figure $35(a)$, just as in figure 34 there is a strong spiral focus corresponding to the leg of the hairpin and an essentially circular contour capturing it. As can be confirmed in figure 33 there are no induced vortex structures in this plane. Figure $35(b)$, taken at $x = 5$, is very near the centre of the head of the hairpin vortex and close to the beginning of the induced vortex's legs.
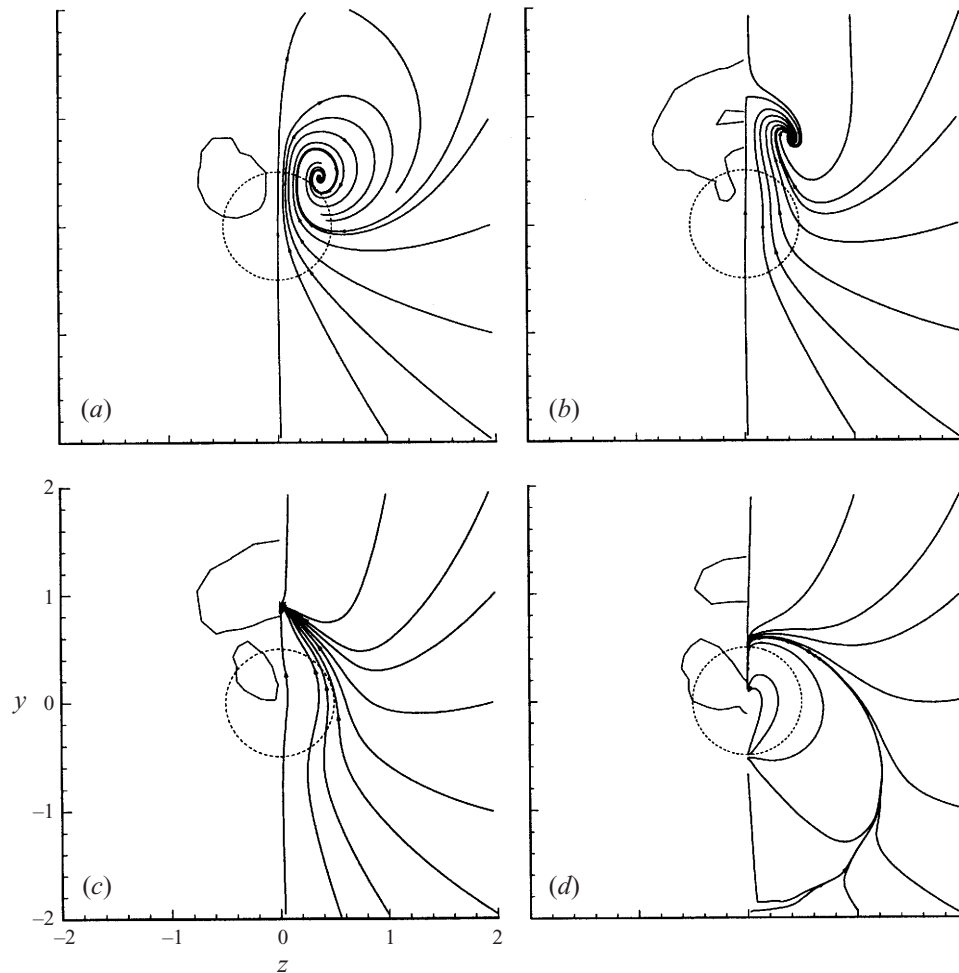
FIGURE 35. Cross-section of the vortical structure and streamlines of projected cross-flow velocity vectors: (*a*) $x = 4$; (*b*) $x = 5$; (*c*) $x = 5.5$; (*d*) $x = 6$.

The vector traces still show the focus of the hairpin's rotation, though its shape has changed slightly. A saddle point, whose separatrix caps the focus, now appears at the intersection of the upward flow between the legs of the hairpin and the far-field flow. Below the focus, the vector traces bend in the vicinity of the sphere's projected area. On the left of the figure, the contour lines show the cross-section of the hairpin vortex's head with a hole in the centre near the saddle point. In addition, there is a small leg extending downward from the head of the vortex in the region of the bending vector traces. Since the hairpin vortex consists of clockwise rotating flow, and the general sense of rotation of the bend is counterclockwise, the small extension is most likely the beginning of the induced hairpin's legs. Figure 35(*c*) is taken at $x = 5.5$, passing through the core of the hairpin's head and slicing through the upstream segment of the induced hairpin's legs. The spiral focus has disappeared into a point node. Below the node, the bend in the vector traces has become stronger. The contours show the head of the hairpin centred just over the node and the legs of the induced hairpin, having increased in size, are now separated from the head of the hairpin. In figure 35(*d*), at $x = 6$, the head of the hairpin has shrunk considerably while the legs of the induced
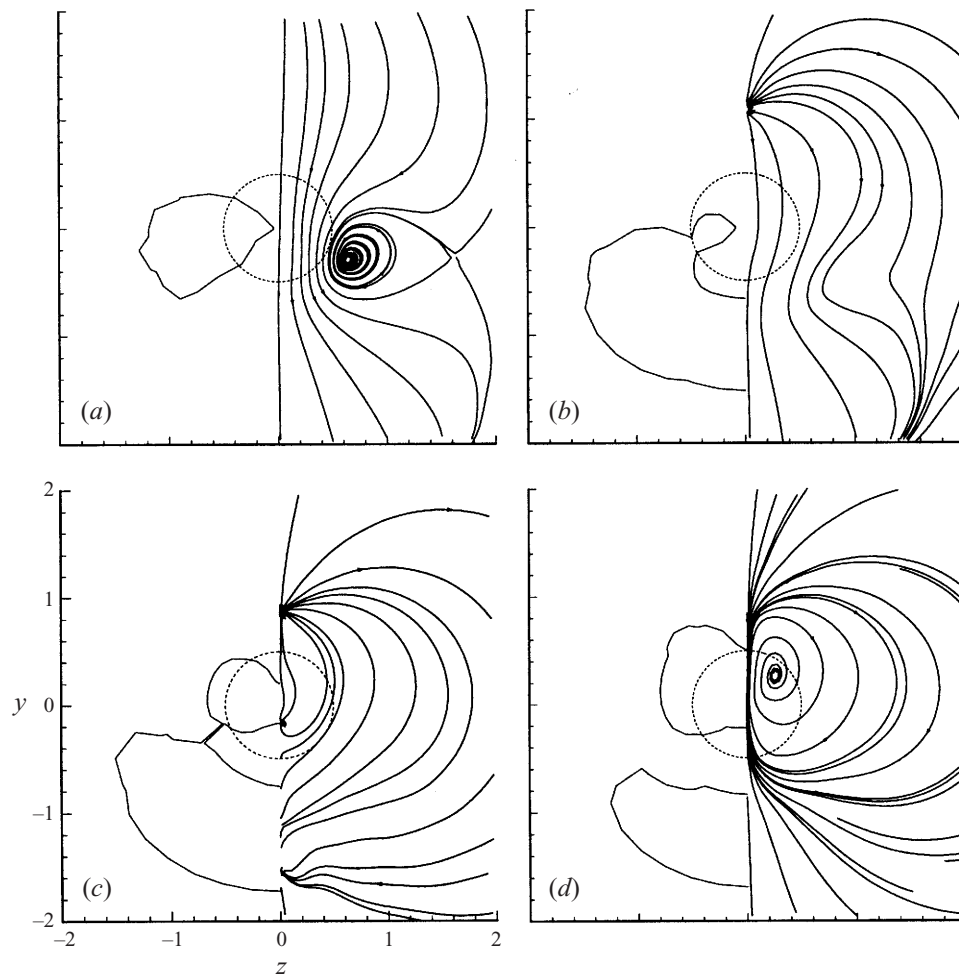
FIGURE 36. Cross-section of the vortical structure and streamlines of projected cross-flow velocity vectors: (a) $x = 7.5$; (b) $x = 8$; (c) $x = 8.5$; (d) $x = 9$.

hairpin have grown. In addition, the vectors along the centreline, below the head of the hairpin, point downward, aligned with the induced velocity between the legs of the induced hairpin.

Figure 36 shows the next sequence of planes at $x = 7.5$, 8, 8.5 and 9, passing through the induced hairpin vortex's head to the legs of the following hairpin. Figure 36(a) shows the plane at $x = 7.5$, approaching the induced hairpin's head. The development from the end of the previous figure at $x = 6$ to here is straightforward: more cross-flow vectors are induced downward by the induced hairpin's legs as they grow to what is seen in figure 36(a). Figure 36(b) shows a plane at $x = 8$. The head of the induced hairpin is clear in the contour lines and the counterclockwise spiral of the induced hairpin's legs has disappeared. In analogous fashion to the previous sequence, there is a clockwise bend in the vector traces and an outgrowth in the contour plot has appeared at $y = 0$, $z = -0.2$, revealing the beginning of the next hairpin's legs. A node at $y = 1.0$ indicates that the next hairpin vortex has already begun exerting its influence on the cross-flow. At $x = 8.5$, in figure 36(c), the clockwise motion of the vector traces has increased and the leg of the hairpin vortex has grown and separated from the head
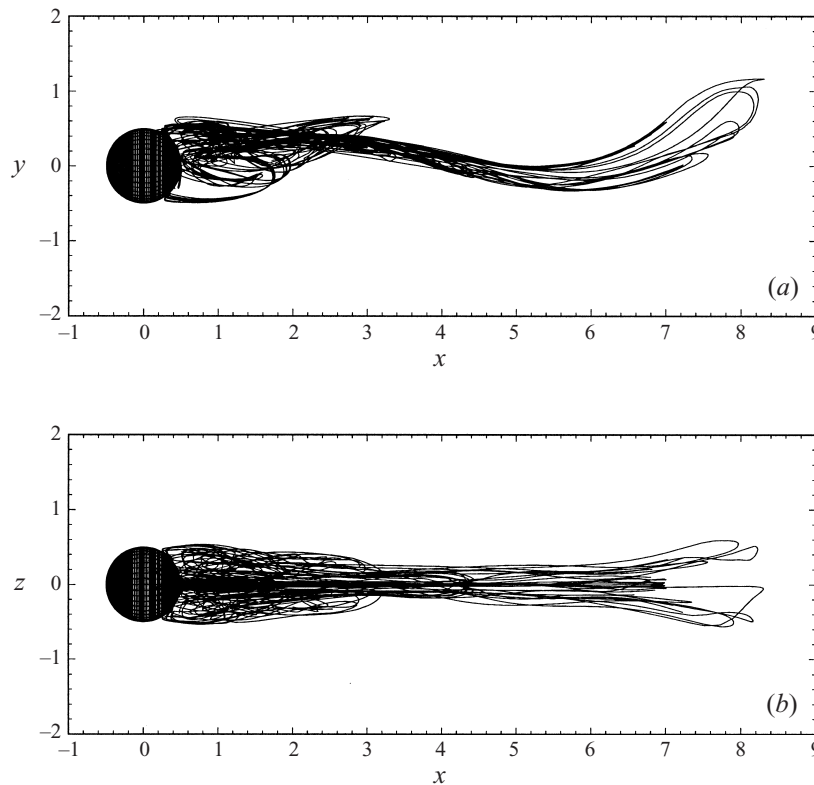
FIGURE 37. Computational streaklines at $Re = 300$ for $\phi = \pi$: (a) $(x, y)$-plane; (b) $(x, z)$-plane.

of the induced hairpin. The small link between the two in the contour plot is, in all likelihood, an artifact of the plotting interpolation. In the final figure of this sequence, figure 36(d) at $x = 9$, the cross-flow pattern has developed as should be expected. The clockwise rotation of the legs of the hairpin vortex has become dominant and the head of the induced hairpin has decreased in size.

### 6.6. *Comparison with experiments*

Figures 35 and 36 show that both the hairpin and induced hairpin vortices exhibit the real physical properties one would expect from a vortex. However, there remains an apparent disparity between the calculated vortex structure shown in figure 30 and the results of flow-visualization experiments attempting to reveal the vortex structure. The sketch in figure 1, for example, from Achenbach (1974) depicts what appears to be one side of the structure shown in figure 30. In addition, dye visualization results presented by Perry & Lim (1978) and Sakamoto & Haniu (1990) show essentially the same structure sketched by Achenbach. In both cases, hairpin vortices are observed shedding with a constant orientation. This one-sided, fixed-orientation shedding of hairpin vortices is seen in all of these experimental studies. Even numerical particle traces, such as those by Shirayama (1992) and by Gebing (1994) reveal one-sided shedding.

It is clear that to compare the current numerical simulations directly to experimental results, instantaneous streamlines, vector traces, and the computed vortex structure are not appropriate. Therefore, figure 37 shows streaklines produced from the numerical simulation viewed normal to the $(x, y)$- and $(x, z)$-planes. A streakline is the locus of points connecting particles released into the flow from a fixed point in the flow field.

Experimentally, streaklines correspond to the results obtained from flow visualizations whereby dye, moving with the sphere, is released from the wake region. The numerical streaklines shown in figure 37 correspond to the flow field at a phase angle of $\phi = \pi$, the designated starting point of the shedding cycle. Therefore, figures 37(a) and 37(b) can be compared with the third panels of figures 30(a) and 30(b). The loops in the streaklines correspond well to the locations of the hairpin vortices revealed by Jeong & Hussain's method. What is most striking though, is the fact that the induced hairpin does not show up in the streaklines. Some limited attempts at repositioning the numerical 'dye ports' were also unsuccessful in capturing the induced hairpins in the streaklines. The fact that the current results simultaneously reveal the alternately shed hairpins using Jeong & Hussain's method and show the experimentally observed one-sided shedding in the streaklines is particularly interesting.

Current experimental flow-visualization results for the shed vortex structure are shown in figures 38 and 39. Figure 38 shows the structure of a shedding hairpin vortex as it extends out of the near wake. This picture clearly shows the physically observed geometry of the vortices and can be compared to the numerically calculated structures in figures 30 and 31. In figure 39 both pictures are taken some time after the sphere has traversed the region and show the wake at approximately 30 diameters downstream of the sphere. Figure 39(a) shows what would correspond approximately to the $(x, y)$-plane in the simulations, although it is slightly rotated and the vertical direction is reversed. Even so, the constant orientation of the shed vortices is plainly evident. The spacing between the vortex heads was measured at just over 6.5 sphere diameters giving a Strouhal number of 0.15. Figure 39(b) corresponds to what would be the $(x, z)$-plane in the simulations. The regularity of the vortex spacing is clear and the vortex spacing was again found to be between 6 and 7 sphere diameters. The most interesting aspect of figure 39 is the small kinks that are present in the legs of the hairpin vortices. This same-style kink is present in the results from Sakamoto & Haniu although it is not depicted in their accompanying sketch. It is likely, from the results presented above, that these kinks develop under the influence of the induced velocity from the induced hairpin vortices. Considering figure 30, it is easy to imagine the induced hairpins causing a spreading and turning of the flow to cause such a feature. A similar kink is present, but only very faintly, in the streakline pattern of figure 37(b) at $x \approx 5$, the correct location to correspond to the head of the induced vortex. It is quite possible that more a refined calculation of the streaklines would show the hairpin kinks in greater detail.

Finally, with what is now known from the numerical results, the experimental observations of the shedding process can be described. Observations from the flow visualizations produced using the method described in §3 reveal a generally less detailed, but equally interesting, picture of the shedding mechanism than that provided by the numerical simulations. Figure 40 shows a picture of the near wake as a hairpin vortex is beginning to shed. The view is equivalent to the $(x, y)$-plane in the numerical results with the $z$-direction reversed. Figure 41 illustrates a complete shedding cycle. The shedding mechanism apparent from experimental observations can be followed by studying these pictures. The photographs in figure 41 were taken at a Reynolds number of 300 and are equally spaced in time from the start of one period to the next. Therefore, the time increment between each photograph is equal to 1/5 of a period. For the experimental conditions one period was roughly 14.5 s. With reference to the numerically defined coordinates, the vantage point in the photographs is approximately 45° above the $(x, z)$-plane, with the orientation of the shed hairpins toward the bottom of the pictures.
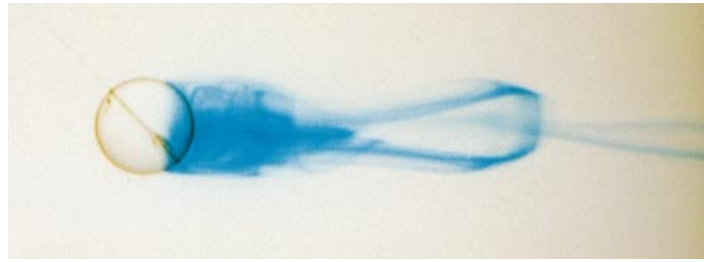
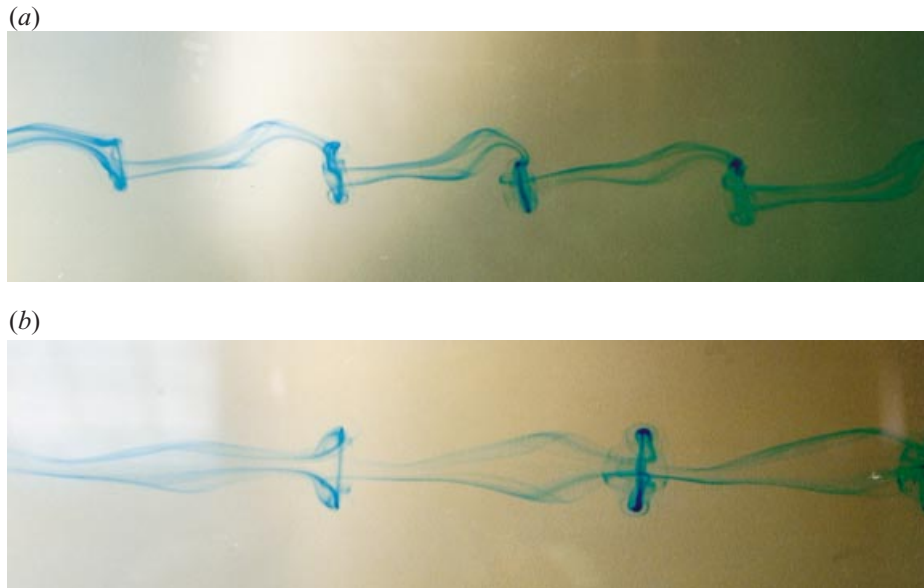FIGURE 38. Dye visualization of a shedding hairpin vortex at $Re = 300$.

(*a*)



(*b*)



FIGURE 39. Two views of dye visualizations of the hairpin vortices in the wake at $Re = 300$:
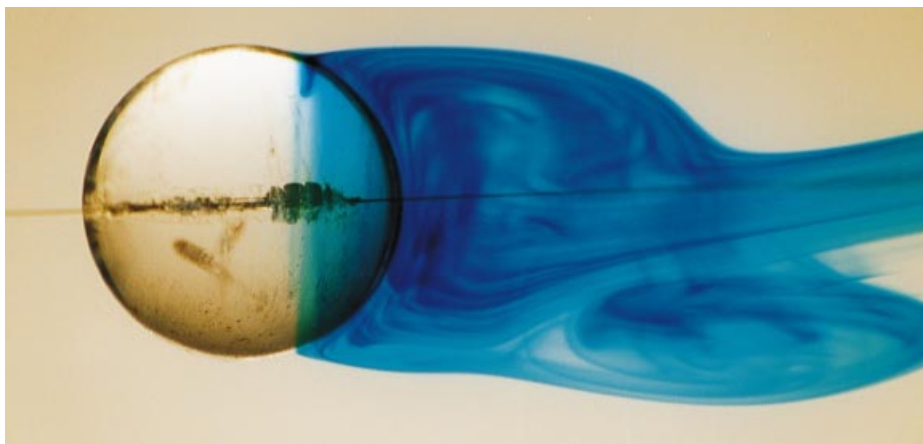(*a*) $(x, y)$-plane; (*b*) $(x, z)$-plane.



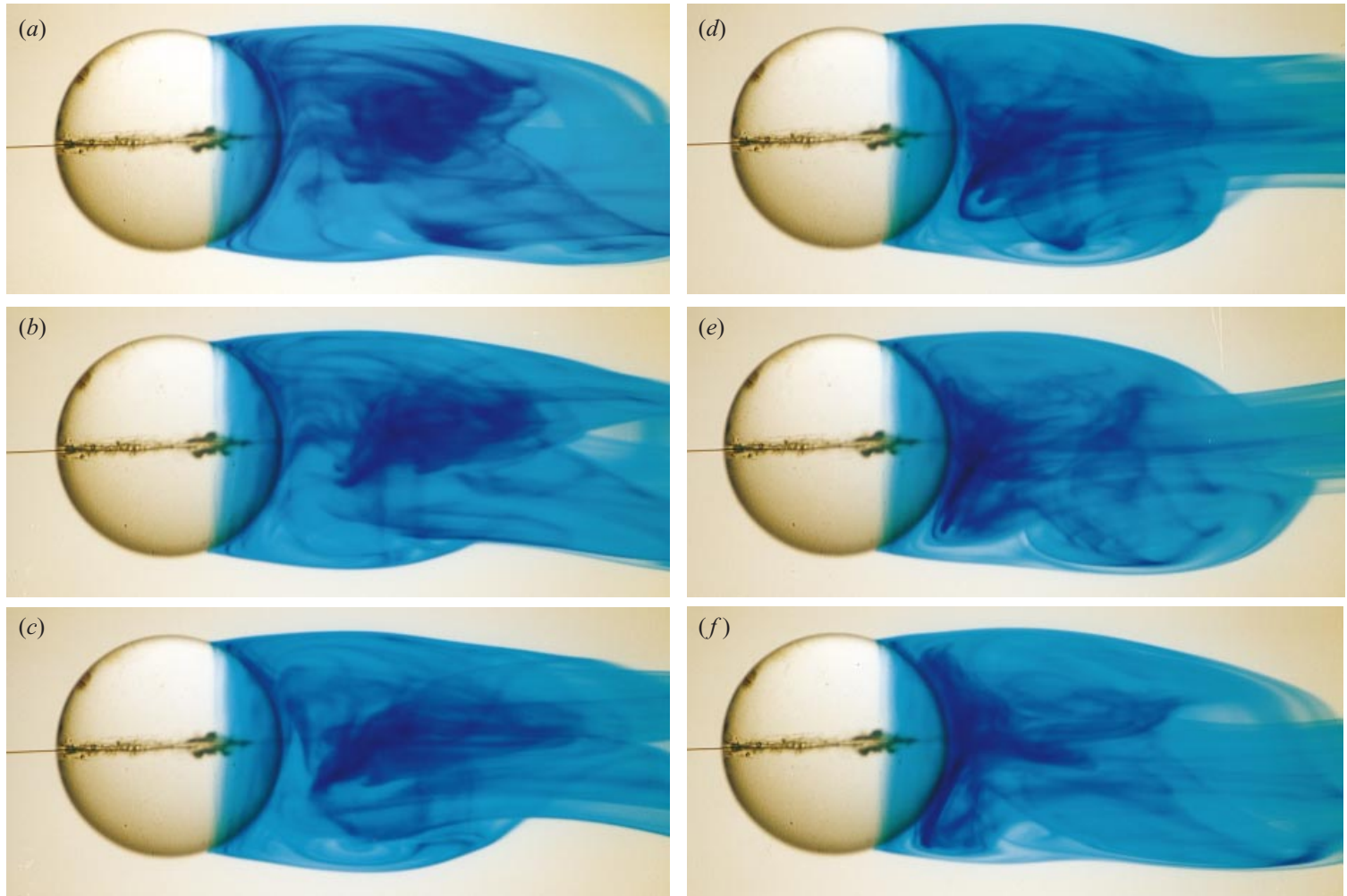FIGURE 40. Dye visualization of the near wake at $Re = 300$.

FIGURE 41. Dye visualization sequence of shedding in the near wake at $Re = 300$: ($a$) $t = 0$; ($b$) $t = T/5$; ($c$) $t = 2T/5$; ($d$) $t = 3T/5$; ($e$) $t = 4T/5$; ($f$) $t = T$.

During the experimentally observed shedding cycle, one side of the vortex ring is seen to move downstream to form the downstream bight of a hairpin vortex. Ignoring for now what are known to be the legs of a previously shed hairpin vortex, this corresponds to the spiralling recirculation seen at the lower right-hand side of figure 40. Note again that the flow in figure 40 is upside down relative to the numerical results where the downstream bight of the hairpin is shed from the top of the wake. Figure 41(*a*) shows the first stage in the shedding cycle. The vortex ring is located about one diameter downstream of the sphere, on the far right side of the photograph. The ring has already tilted and the downstream bight is moving out of view. As the downstream bight of the vortex sheds and proceeds farther downstream to form a hairpin-shaped vortex, the legs of the hairpin remain in the near wake and are seen to stretch and move closer together and toward the axis. As they move toward the axis, they can be seen becoming enveloped in the shear layer which surrounds the near wake and from which they themselves originated. In figure 41(*b*) the downstream bight has just moved out of the picture and the shear layer is beginning to envelop the legs of the hairpin. This is particularly evident in the slight jog in the lower surface of the wake boundary. At this point the upstream bight of the shed hairpin vortex, adjacent to the rear surface of the sphere, appears to move across the wake. In figure 41(*c*), as unlike 41(*b*), the legs of the shed hairpin curve downward as they extend into the near wake. This stage is also well represented in figure 40, which shows the legs of a previously shed hairpin extending into the near wake and appearing to originate from the lower half of the wake. Recall from figure 41(*a*) that the legs remain connected to the upstream bight. The upstream bight of the hairpin, which is known to have begun on the top side of the wake, has therefore moved to the lower half of the figure. With reference to figure 27, which shows (*x, y*)-cross-sectional contours of *z*-vorticity, this cross-wake movement of the upstream bight is represented in the last panel in the figure where positive vorticity from the lower half of the wake tears from the rest of the shear-layer vorticity. It is this cross-wake move of the upstream bight which, during flow visualizations, appears to be responsible for separating the next hairpin in the sequence.

In figures 41(*c*) to 41(*f*) this process is seen in discrete steps. In figure 41(*c*) the upstream bight has crossed to the bottom of the wake where there is new vortex forming out of the shear layer. In figure 41(*d*) the new vortex on the lower side of the wake has grown and moved a bit downstream. By figure 41(*e*), the new vortex has completely formed and can be seen encircling the legs of the previous hairpin. It is in figure 41(*e*) that the cycle has reached the stage where the lower section of the new vortex is being separated from the near wake by the upstream bight of the previous vortex. By the final figure, figure 41(*f*), the flow has essentially returned to the state shown in figure 41(*a*) with the next vortex beginning to shed. The complete cycle suggests a mechanism not unlike, though lacking the details, of that indicated by the numerical results.

The upstream bight, which originates from the top of the shear layer in figure 41, consists of clockwise rotating flow. When it moves to the bottom of the wake, intuitively under the effect of the self-induced velocity of the highly curved bight and the corotating legs of the hairpin, it interacts with and dissipates counterclockwise rotating flow in the lower half of the shear layer. This interaction process is then responsible for cutting the next hairpin free from the shear layer to restart the process. The consistent orientation of the shed vortices can then be associated with the self-induced cross-wake movement of the upstream bight.

This view of the shedding process can be seen as closely related to that given by

Gerrard (1966) for the shedding behind circular cylinders, where vorticity is induced across the wake to release a vortex from the opposite side. However, as the current work clearly shows, a mechanism obtained solely from experimental observations is, by definition, completely phenomenological and ignores critical features of the three-dimensional process such as the azimuthal flow and pressure gradient effects on the evolution of the vortices as well as the generation and presence of the induced hairpin vortices.

## 7. Conclusions

The present study was undertaken with the objective of numerically simulating and analysing in detail the first three flow regimes of the flow past an isolated sphere, namely steady axisymmetric flow, steady non-axisymmetric flow, and unsteady periodic flow. Of primary interest was defining the kinematics of the flows and the transition processes between regimes. The final goal of the work was to be a cross-regime description of the flow evolution from symmetry breaking to temporal instability.

The results showed flow separation occurring at a Reynolds number of 20 and the wake was found to consist of a toroidal vortex. These are results consistently reported in previous studies. However, in pursuing a more in-depth analysis of the flow field, the vortex is found to be balanced at these low Reynolds numbers by viscous forces, as opposed to radial pressure gradients. With increasing Reynolds number, pressure effects are shown to become increasingly important. By $Re = 200$, the centrifugal acceleration of the wake vortex is seen to be balanced by a local pressure minimum within its core as the viscous effects become less dominant. The structure of the wake vortex, which is fairly straightforward in this regime, was best elucidated not by vorticity contours, but rather by the method proposed by Jeong & Hussain (1995) which targets swirling motions around local pressure minima.

Concurrent with the shift of the wake vortex from viscous to pressure gradient effects, the transition to the second flow regime is observed. At a Reynolds number of 211, the axial symmetry of the flow is seen to break down. The resulting flow, however, still preserves reflection symmetry and temporal stability. The computed onset of this regime is in excellent agreement with previous experimental and numerical results which put the transition at $210 < Re < 212$. It appears that the transition is associated with an azimuthal instability of the low-pressure core of the toroidal vortex. The instability grows as the viscous effects in the vortex become increasingly less important. Based on this supposition, a mechanism describing the transition is proposed. An azimuthal pressure gradient resulting from the instability drives flow through the vortex core and opens up the once closed separation region to the entrainment and release of fluid. The release of wake fluid occurs through two tails, in agreement with the double-thread wake first observed in liquid drop experiments by Magarvey & Bishop (1961). The vortex structure of the wake clearly shows two streamwise vortices extending downstream. Contours of the streamwise vorticity component compare well to the isosurface calculated by Tomboulides (1993). The experimental flow visualization results of the current study were found to compare quite well to particle traces from the numerical simulation.

Using the full unsteady capabilities of the numerical method, steady solutions for the flow were found up to a Reynolds number of 270. At $Re = 280$ the results were clearly periodic. The current results, therefore, agree with the experimental results of Magarvey & Bishop (1961) who reported the onset of unsteadiness at $Re = 270$.

Comparisons with previous numerical investigations are also favourable. Although strictly applicable only to the axisymmetric base flow, the stability analysis by Natarajan & Acrivos (1993) indicates a Hopf bifurcation at $Re = 277.5$. Tomboulides (1993) found the transition from the physically observed non-axisymmetric base flow in the range $270 < Re < 285$. At $Re = 300$ computed flow variables also compare well with previous results to the extent that they are available. The computed Strouhal number of 0.137 is in remarkable agreement with that of Tomboulides at 0.136. The current study's experimentally determined Strouhal number range of 0.148–0.165 is slightly higher, as generally appears to be the case with experimental results: Sakamoto & Haniu (1990) found a range of 0.15–0.165. The calculated drag coefficient of 0.656 lies between the experimental results of Roos & Willmarth (1971) at 0.629 and the numerical results of Tomboulides at 0.671.

The mechanism proposed above for the breakdown of axial symmetry is extended to describe the transition to unsteadiness. The unsteady flow is seen to be driven by the periodic growth of the wake vortex and its release from and subsequent regeneration within the near-wake region. The vortical structure of the wake shows not only the periodic hairpin vortices shed with consistent orientation as revealed by flow visualizations, but also previously unrevealed, oppositely oriented hairpin vortices induced by the interaction of the near-wake flow and the outer flow. These newly visualized vortex structures support an intuitive understanding of the shedding process showing a reaction of the flow field to the previously revealed one-sided hairpins. The presence of the induced hairpin vortices clarifies the points raised in the introduction regarding the structure of the wake. In particular, it becomes clear that the transverse circulation of the wake is bounded with the induced vortices opposing the effect of the standard hairpins. In addition, the topological inconsistencies of figure 1 are avoided with hairpins connected to induced hairpins rather than to each other. Correctly capturing the vortical structure of the wake is clearly required for a firm understanding of the physics. Numerical streaklines, however, help to validate the computed results by mimicking the experimental flow visualizations and revealing only the hairpins generated in the interior of the wake. This point highlights the importance of understanding the limitations of the tools of both experimental and numerical analysis.

Finally, as a complement to the shedding mechanism implied by the details of the numerical results, a phenomenological mechanism is put forth based on the experimental flow visualization results. Here, one loop of the wake vortex is shed downstream while the other loop moves under its self-induced velocity field across the wake to cut the next vortex loop free. While this mechanism is intuitively appealing, it is important to be aware of the whole picture, as supplied by the numerical results.

## REFERENCES

ACHENBACH, E. 1974 Vortex shedding from spheres. *J. Fluid Mech.* **62**, 209–221.

ALLEN, H. S. 1900 The motion of a sphere in a viscous fluid. *Phil. Mag.* (5) **50**, 323–338; 519.

BEAM, R. & WARMING, R. F. 1978 An implicit factored scheme for the compressible Navier–Stokes equations. *AIAA J.* **16**, 393–402.

CHONG, M. S., PERRY, A. E. & CANTWELL, B. J. 1990 A general classification of three-dimensional flow fields. *Phys. Fluids* A **2**, 765.

GEBING, H. 1994 Numerische Simulation und topologish-physikalishe Analyse der instationären, dreidimensionalen, abgelösten Wirbelströmungen an einer Kugel und an Rotationsellipsoiden. PhD Thesis, Georg-August-Universität Göttingen.

GERRARD, J. J. 1966 The mechanics of the formation region of vortices behind bluff bodies. *J. Fluid Mech.* **190**, 265–298.

HUNT, J. C. R., WRAY, A. A. & MOIN, P. 1988 Eddies, stream, and convergence zones in turbulent flows. *Center for Turbulence Research Rep.* CTR-S88.

JEONG, J. & HUSSAIN, F. 1995 On the identification of a vortex. *J. Fluid Mech.* **285**, 69–94.

JOHNSON, T. A. 1996 Numerical and experimental investigation of flow past a sphere up to a Reynolds number of 300. PhD Thesis, The University of Iowa.

KIM, H. J. & DURBIN, P. A. 1988 Observations of the frequencies in a sphere wake and of drag increase by acoustic excitation. *Phys. Fluids* **31**, 3260–3265.

LIEBSTER, H. 1927 Über den Widerstand von Kugeln. *Ann. Physik* **82**, 541–562.

MAGARVEY, R. H. & BISHOP, R. L. 1961 Transition ranges for three-dimensional wakes. *Can. J. Phys.* **39**, 1418–1422.

MAGNAUDET, J., RIVERO, M. & FABRE, J. 1995 Accelerated flows past a rigid sphere or a spherical bubble. Part 1. Steady straining flow. *J. Fluid Mech.* **284**, 97–135.

NAKAMURA, I. 1976 Steady wake behind a sphere. *Phys. Fluids* **19**, 5–8.

NATARAJAN, R. & ACRIVOS, A. 1993 The instability of the steady flow past spheres and disks. *J. Fluid Mech.* **254**, 323–344.

PERRY, A. E. & LIM, T. T. 1978 Coherent structures in coflowing jets and wakes. *J. Fluid Mech.* **88**, 451–463.

PERRY, A. E., LIM, T. T. & CHONG, M. S. 1980 The instantaneous velocity field of coherent structures in coflowing jets and wakes. *J. Fluid Mech.* **101**, 243–256.

PRUPPACHER, H. R., LE CLAIR, B. P. & HAMILIEC, A. E. 1970 Some relations between drag and flow pattern of viscous flow past a sphere and a cylinder at low and intermediate Reynolds numbers. *J. Fluid Mech.* **44**, 781.

ROOS, F. W. & WILLMARTH, W. W. 1971 Some experimental results on sphere and disk drag. *AIAA J.* **9**, 285–291.

SAKAMOTO, H. & HANIU, H. 1990 A study on vortex shedding from spheres in a uniform flow. *Trans. ASME: J. Fluids Engng* **112**, 386–392.

SAKAMOTO, H. & HANIU, H. 1995 The formation mechanism and shedding frequency of vortices from a sphere in uniform shear flow. *J. Fluid Mech.* **287**, 151–171.

SCHILLER, L. 1930 *Stickholmer Vortäge*, vol. 1, pp. 226–233.

SCHLICHTING, H. 1979 *Boundary-Layer Theory*, 7th edn. McGraw-Hill.

SCHMIEDEL, C. 1928 Experimentalle Untersuchungen über die Fallbewegun von Kugeln und Schieben in reibenden Flüssigkeiten. *Physik. Z.* **29**, 593–610.

SHIRAYAMA, S. 1992 Flow past a sphere: topological transitions of the vorticity field. *AIAA J.* **30**, 349–358.

SOTIROPOULOS, F. & ABDALLAH, S. 1991 The discrete continuity equation in primitive variable solutions of incompressible flow. *J. Comput. Phys.* **95**, 212–227.

TANEDA, S. 1956 Experimental investigation of the wake behind a sphere at low Reynolds numbers. *J. Phys. Soc. Japan* **11**, 1104–1108.

TOBAK, M. & PEAKE, D. J. 1982 Topology of three-dimensional separated flows. *Ann. Rev. Fluid Mech.* **14**, 61–85.

TOMBOULIDES, A. G. 1993 Direct and large-eddy simulation of wake flows: flow past a sphere. PhD Thesis, Princeton University.

TOMBOULIDES, A. G., ORSZAG, S. A. & KARNIADAKIS, G. E. 1993 Direct and large-eddy simulation of axisymmetric wakes. *AIAA Paper* 93-0546.

VAN DYKE, M. 1982 *An Album of Fluid Motion*. Parabolic Press, Stanford, CA.

WIESELBERGER, C. 1922 Weiter Feststellungen über die Gesetze des Flüssigkeits- und Luft-widerstandes. *Physik. Z.* **23**, 219–224.

WILLIAMSON, C. H. K. 1996 Three-dimensional wake transition. *J. Fluid Mech.* **328**, 345–407.

WINNIKOW, S. & CHAO, B. T. 1966 Droplet motion in purified systems. *Phys. Fluids* **9**, 50–61.